2009-01-01

High Temperature Oxidation Behavior of Nb-20Mo-15Si-5B-20Cr Alloy

Julieta Angelica Ventura
University of Texas at El Paso, javentura@miners.utep.edu

HIGH TEMPERATURE OXIDATION BEHAVIOR OF Nb-20Mo-15Si-5B-20Cr ALLOY

JULIETA ANGELICA VENTURA

Department of Metallurgical and Materials Engineering

APPROVED:

S.K. Varma, Ph.D., Chair

Luis Trueba, Ph.D.

Stella A. Quinones, Ph.D.

Patricia D. Witherspoon, Ph.D.
Dean of the Graduate School

Dedicated to my parents, Raul & Rosa
and to my sisters, Grisel & Tania.

HIGH TEMPERATURE OXIDATION BEHAVIOR OF Nb-20Mo-15Si-5B-20Cr ALLOY

By

JULIETA ANGELICA VENTURA, B.S.M.E

THESIS

Presented to the Faculty of the Graduate School of

The University of Texas at El Paso

in Partial Fulfillment

of the Requirements

for the Degree of

MASTER OF SCIENCE

Department of Metallurgical and Materials Engineering

THE UNIVERSITY OF TEXAS AT EL PASO

May 2009

ACKNOWLEDGMENTS

I would like to express my sincere gratitude to my advisor Dr. S.K. Varma for giving me the opportunity to do research in the high temperature oxidation field. Thanks Dr. Varma for his guidance and support. I would also like to thank Dr. Luis Trueba and Dr. Stella Quinones for accepting to be part of my committee. Special thanks to Dr. Murr, who gave me the opportunity to pursue my graduate studies in the Metallurgical and Materials Engineering field. His help and support are highly appreciated. I gratefully acknowledge the financial support given by the Metallurgical and Materials Engineering Department and the Office of Naval Research (ONR) through the award number DN00014-08-1-0506 and project number 08PR03729-00.

I want to thank Mr. David Brown for helping the research team and for the setup of high temperature furnaces and other equipment. Without his help, this research would not have been completed. I would also want to thank Dr. McClure for all his help with the SEM and XRD instruments and Dr. Ramana for his support with the SEM.

Special thanks to my co-workers, friends and family for their help, friendship and support. Thanks Pilar and Ben for sharing all your knowledge with me. Thanks to Karina and Lucet for their advice and guidance and to my sister Grisel for her constant motivation, and for helping me with the schematics. To my parents, Raul and Rosa; thanks for your guidance, advice, support, encouragement and for being my role models.

ABSTRACT

Materials for high temperature applications, such as jet engines, gas turbines and turbine blades, require a balanced combination of physical and chemical properties to withstand the aggressive environments in which they are utilized. Some of the properties required are high strength, low density, high melting point and good oxidation resistance at elevated temperatures [1-3]. For this reason, the microstructure and oxidation behavior of the Nb-20Mo-15Si-5B-20Cr alloy (at. %) has been studied as a potential candidate to replace nickel-based alloys currently used in the aerospace industry.

Short term oxidation (STO) and long term oxidation (LTO) studies have been performed in air for this alloy over a temperature range from 700℃ to 1400℃, for 24 and 168 hours respectively. Oxidation curves for this alloy were obtained by plotting the mass gain per unit area as a function of temperature and time to determine its oxidation resistance. STO was temperature dependent and oxidation curve shows a minimum mass gain per unit area between 900 and 1000℃. LTO was time dependent and curves show a minimum mass gain at 1200 and 1300℃. Parabolic behavior was observed at those temperatures.

Microstructure of the alloy and oxidized products were characterized using X-ray diffraction (XRD), scanning electron microscopy (SEM) and energy dispersive spectroscopy (EDS). According to results, the microstructure is composed of body center cubic (BCC) solid solution (α), tetragonal Nb_5Si_3, Nb_3Si, hexagonal Laves phase $NbCr_2$ and a eutectic like microconstituent α, Nb_3Si and $NbCr_2$. The oxidation products

at 700 to 1300°C show the presence of Nb_2O_5, SiO_2, $CrNbO_4$, among others. The parabolic and linear oxidation rate constants values indicate that the studied alloy is competitive when compared to the values for Nb-based alloys reported by different authors.

TABLE OF CONTENTS

LIST OF FIGURES

LIST OF TABLES

CHAPTER 1

INTRODUCTION

Materials for high temperature applications, such as jet engines, gas turbines and turbine blades, require a balanced combination of mechanical and chemical properties to withstand the aggressive environments in which they are utilized. Some of the properties required are high strength, low density, high melting point and good oxidation resistance at elevated temperatures [1]. Currently, the aerospace industry utilizes nickel-based super alloys to manufacture these aircraft components. However, in past years, working temperatures of these engines have been increasing and they are approaching the limit of nickel-based superalloys (1150℃). For this reason, new metallic systems and alloys that can survive above the 1150℃ are investigated [1-3].

Niobium silicide-based alloys are studied as potential candidates to replace nickel super alloys because of their high melting point (~1750℃), low density (6.6 to 7.2 g/cc) and high temperature strength [1,4] however their poor oxidation resistance at elevated temperatures prevents them use for various applications. Studies have shown that additions of alloying elements such as chromium, titanium, aluminum, molybdenum and hafnium to these alloys improve their oxidation resistance at temperatures up to 1300˚C due to the formation of intermetallic phases [3, 5-8]. Among the alloying elements, Cr is the most promising because it promotes the formation of Laves phase $NbCr_2$ [1, 9-15]

The alloy considered in this study is the Nb-20Mo-15Si-5B-20Cr (composition given in atomic percent). The composition of the alloy was given by Naval Air Warfare Center and it relies on the basis for developing oxidation resistant microstructures. The

addition of silicon promotes the formation of niobium silicides Nb_5Si_3 and Nb_3Si while chromium provides the Laves phase $NbCr_2$ to the alloy. These additions improve the oxidation resistance of the alloy. Boron is added as a phase stabilizer. The addition of molybdenum strengths the solid solution of niobium Nb_{ss} and provides the tensile ductility and fracture resistance at room temperature to the alloy.

The purpose of this research is to study the oxidation behavior of the Nb-20Mo-15Si-5B-20Cr alloy in a temperature range from 700 to 1400°C. The effect of oxidation temperature and time has been studied as well as the effect of alloying elements during exposure. Previous research has been performed on Nb-W-Cr systems with B and C modifiers to understand the oxidation behavior of single-phase and two-phase ternary alloys. This study has a similar approach to study the oxidation behavior of a multi-phase niobium based alloy.

CHAPTER 2

BACKGROUND

2.1 Oxidation Principles

Engineering metals and alloys react chemically when exposed to air especially at high temperatures because the susceptibility of the metal to chemical attack increases with increasing temperature. The most common reactant is the air or oxygen, therefore this chemical reaction is called oxidation. Oxidation is defined as the interaction of the metal with the oxygen producing an oxide [16]. The oxidation mechanisms, which a metal or alloy can be subjected to, are as follows:

1. Metal surface adsorbs atomic oxygen.
2. Oxide nucleates at multiple sites that are thermodynamically favorable and grows to form a continuous film.
3. As the oxide layer grows it provides a protective scale that prevents the metal from further oxygen attack.
4. Growth stresses develop cracks and porosity in the oxide that modify the oxidation mechanism and may cause failure to protect the metal from the oxygen.

There are three main laws by which the metal or alloy oxidizes at high temperatures: linear, parabolic and logarithmic. At high temperatures, metals and alloys have a combination of linear and parabolic oxidations. Linear oxidation occurs when the metal's surface is not protected by a layer of oxide; with prolonged time exposure the metal would continue to oxidize at a constant rate and it would never slow down causing

the destruction of the metal. Several factors cause linear oxidation: the formation of volatile or molten oxides, the spallation or breakaway of oxides due to growth and internal stresses or the growth of porous non protective oxide. Parabolic oxidation is controlled by the diffusion of atoms and the driving force is the chemical potential. If a compact oxide layer is formed and it continues to grow at prolonged time exposure, the diffusion distance of atoms increases causing a decrease in the diffusion rate. Most metals and alloys exhibit parabolic behavior at elevated temperatures. This type of oxidation is of great importance because the oxide growth occurs with a decreasing oxidation rate. Logarithmic behavior is observed at the initial stage of oxidation of metals at low temperatures, where a thin oxide layer is formed. It is characterized by a rapid rate of reaction at the beginning of the process followed by a decrease in rate or vice versa [16-18].

2.1.1 Protective Oxides and Oxide Volatilization

Oxide morphology depends on the environment, exposure time and composition of the metal or alloy. It is desirable to have a protective oxide that is adherent, slow forming and self-healing [18]. Some oxides have this protective nature, such as Cr_2O_3, Al_2O_3 and SiO_2 because they are slow growing, dense and chemically stable. At temperatures up to ~1000℃ Cr_2O_3 is very stable and resists oxidation. At higher temperatures Cr_2O_3 transforms to CrO_3 and volatilizes [12, 13, 20-22]. However, it is been reported that the presence of Cr_2O_3 at 1100℃ occurs as a result of oxide entrapment in the oxide scale [9-11]. The volatilization of oxides is an important issue particularly at high temperatures. Molybdenum, tungsten and boron oxides are known

for their volatile behavior and low melting point. Molybdenum oxide MoO_3 sublimes at 704°C and it starts to vaporize above 500°C [18, 23]. Even though the presence of MoO_3 at higher temperatures is not expected, Semmel [24] observed the formation of MoO_3 in pure Mo oxidized from 900-1300°C during the cooling period.

2.2 Refractory Metals and their Intermetallics

The refractory metals are characterized by the high strength of their interatomic bond which provides high melting point, mechanical strength and electrical resistance. Among them, niobium and molybdenum are the most promising refractory metals for high temperature applications. Niobium has a combination of high strength, ductility, low density and high melting point. Molybdenum also has high melting point, higher density, low coefficient of linear thermal expansion and good heat resistance [25]. Table 2.1 summarizes some of the physical properties for niobium and molybdenum.

Table 2.1. Physical properties of niobium and molybdenum [25-26]

Property	Niobium	Molybdenum
Crystal structure	BCC	BCC
Melting point, ˚C	2496	2623
Density, g/cc	8.57	10.2
Young's modulus, 10^6 psi	16	42
Coefficient of thermal expansion 10^{-6} /˚C	7.1	5.4
Ductile-to-brittle transition temp, ˚C	-120	-20

However, both niobium and molybdenum exhibit poor oxidation at elevated temperatures in their monolithic form and they depend on their intermetallic phase to

improve the oxidation resistance [1, 2, 27]. Intermetallic compounds are usually stoichiometric; possess high strength and low deformability at low temperatures. Current efforts are focused in the development of multiphase niobium alloys with solid solutions and substantial amounts of refractory intermetallics such as niobium silicides (Nb_3Si, Nb_5Si_3), borosilicides (Mo_5SiB_2, $Nb_5Si_3B_2$) and Laves phase ($NbCr_2$) [12].

2.2.1 Solid Solutions

As mentioned before, alloys containing niobium silicides also contain solid solutions for toughness and ductility and intermetallics for oxidation resistance. When compared to other refractory metals, niobium retains its ductility even when it is highly alloyed with other metals and it is less susceptible to interstitial impurities. The strengthening of niobium alloys is due to the formation of substitutional solid solutions and studies show that at 1095℃ the most effective strengthening elements are molybdenum, tungsten, vanadium, and zirconium [25].

2.2.2 Niobium Silicides, Nb_5Si_3 and Nb_3Si

The addition of silicon to niobium improves the creep and oxidation resistance at elevated temperatures, typical additions ranges from 12 to 25 at % [1, 2]. The principles for niobium silicide formation rely on the Nb-Si binary system shown in Figure 2.1. In this niobium rich portion there are five stable phases present: liquid (L), Nb, Nb_3Si, β-Nb_5Si_3 and α-Nb_5Si_3. At a composition of ~18 % Si Nb_3Si is formed by a eutectic reaction $L \leftrightarrow Nb+Nb_3Si$ at 1932℃; this silicide has a tetragonal Ti_3P-type crystalline structure. With further cooling, α-Nb_5Si_3 is formed by a eutectoid reaction $Nb_3Si \leftrightarrow Nb+$

α-Nb_5Si_3 at 1700℃; α-Nb_5Si_3 has a tetragonal Cr_5Si_3-type crystalline structure. There is also third reaction Nb_3Si+β-Nb_5Si_3↔α-Nb_5Si_3 at 1946℃.

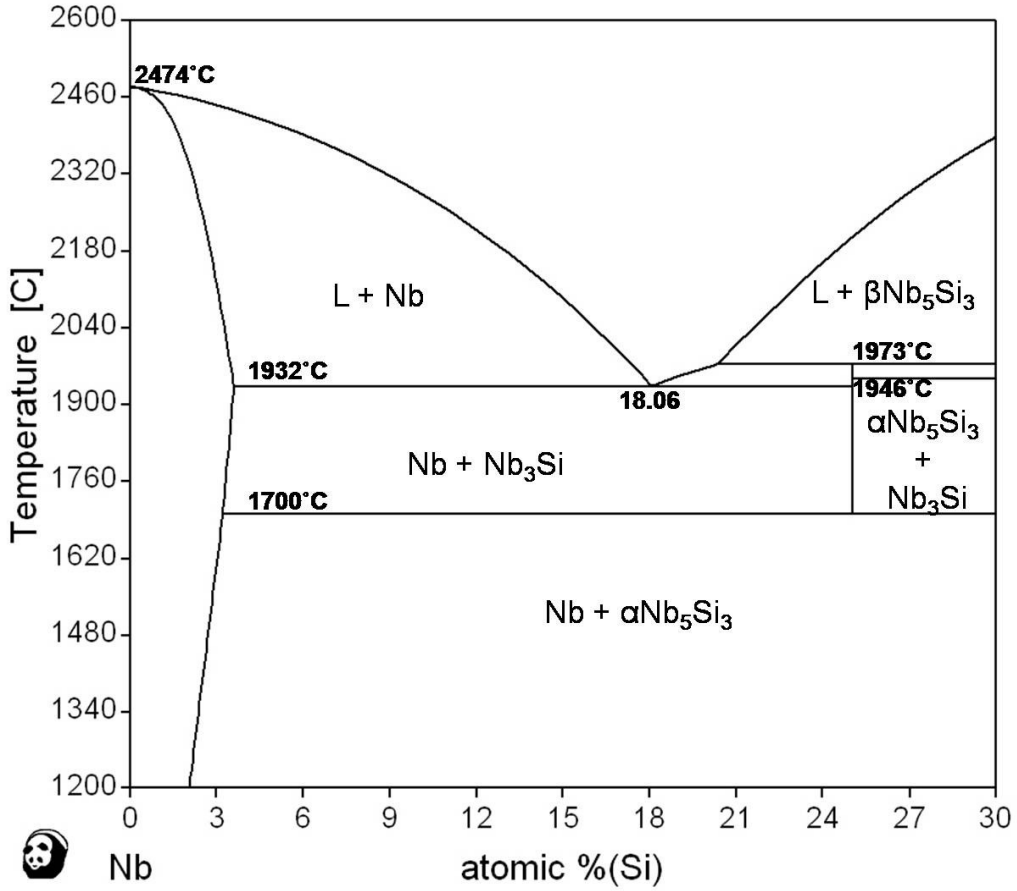

Figure 2.1. Binary phase diagram for Nb-Si system calculated using Pandat™ 8.1 software [28].

Silicides α-Nb_5Si_3 and β-Nb_5Si_3 have a tetragonal crystal structure. The differences between these two phases rely on their lattice parameters (α-Nb5Si3 a: 6.5698Å c: 11.887Å, β-Nb5Si3 a: 10.028Å c: 5.0698Å) and composition. However, the stoichiometry range for both phases is less certain [29, 30]. Nb_3Si has a tetragonal structure. The equilibrium microstructure of niobium-silicide based alloys consists of niobium solid solution and α-Nb_5Si_3. Several authors reported the presence of Nb_3Si

and β-Nb_5Si_3 in the as cast microstructure of alloys with 18 at.% Si [3, 5, 7, 31, 32]. Chan et al. [12] showed the possible presence of Nb_3Si in the microstructure of multiphase alloys. The silicon addition to these alloys ranged from 1.0-17.3 at. %. Geng et al. [5] reported the presence of Nb_3Si and β-Nb_5Si_3 phases in the Nb–18Si–5Al–5Cr–5Mo as cast alloy. After heat treatment, β-Nb_5Si_3 transformed into α-Nb_5Si_3 but Nb_3Si was still present. The author concluded that the presence of Nb_3Si in the heat treated alloy at 1500℃ for 100 hr indicated equilibrium microstructure was not reached. Equilibrium microstructure was observed when the alloy underwent a heat treatment of 200 hr at 1500℃.

2.2.3 Laves Phase, $NbCr_2$

Chromium is a common alloying element because it improves the oxidation resistance of a metal at high temperature. Its melting point (1845-1903℃), low density (7.15g/cc) and its resistance to deformation at elevated temperatures makes it suitable for high temperature applications [15, 33]. The addition of Cr improves the oxidation resistance of niobium silicides by stabilizing the Laves phase ($NbCr_2$) [1, 2, 5, 34]. It has been shown that additions of chromium greater than ~5 at. % stabilizes the chromium-rich Laves phase [1-5]. Laves phases with an AB_2 stoichiometry are the most common intermetallic compounds, as shown by Nb-Cr binary phase diagram in Figure 2.1. There are 3 types of Laves phases: Low temperature cubic C-15 structure ($MgCu_2$-type), high temperature hexagonal C-14 ($MgZn_2$-type), which is only stable at temperatures above ~1624˚C, and the dihexagonal C-36 ($MgNi_2$-type) [34-36]. The equilibrium microstructure consists of chromium or niobium rich solid solutions and C-15

$NbCr_2$. Thermodynamic modeling from the Nb-Si-Cr system as well as experimental studies on alloys from the Nb-Ti-Si-Al-Cr-Mo-Hf system has shown the presence of the C-14 Laves phase $NbCr_2$ in the as cast microstructure. Researchers attributed the phase stabilization to the presence of silicon [3, 5, 6-8, 12, 14, 15, 37-39]. Zhao et al. [15] reported the stabilization of C-14 phase at lower temperatures promoted by silicon; its stability ranges from ~6 to ~26% Si. It also was reported that the C-14 Laves appears with variable Si/Cr concentration but with little variation in niobium. Geng et al. [3,5,7,8] reported the presence of C-14 Laves phase in heat treated samples from the Nb-Si-Al-Cr system at 1000 and 1500°C.

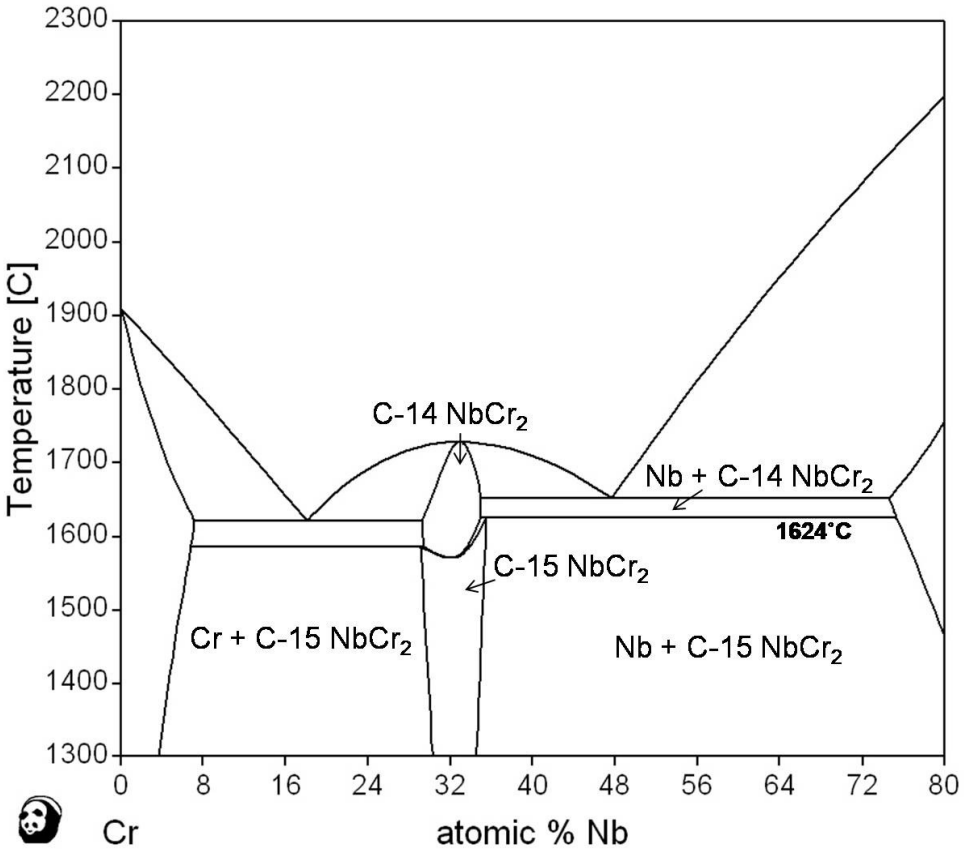

Figure 2.2. Binary phase diagram for Nb-Cr system calculated using Pandat™ 8.1 software [28].

2.2.4 Mo Silicides and Borosilicides

Molybdenum silicides are also potential intermetallics for high temperature applications due to its strength retention and high melting point. $MoSi_2$ is a widely used compound in the heating elements of furnaces. It provides good oxidation resistance up to 1700°C by developing a SiO_2 layer; however, its low creep strength at high temperature and poor fracture toughness are its limitations. The addition of boron to the Nb-Si and Mo-Si systems creates ternary intermetallics such as Nb_5Si_2B and Mo_5SiB_2 and $Mo_5Si_3B_x$. It has been shown that as little as 6.5 at. % of boron addition to alloys from the Mo-Si-B system improves the oxidation resistance and creep resistance of these alloys over monolithic Mo_5Si_3 [40]. Several authors have focused their attention to develop Mo-Si-B silicide alloys because Mo_3Si and Mo_5SiB_2 have melting points on the order of 2000°C and have potential as high temperature structural materials. When combined with molybdenum solid solution, the fracture toughness and creep resistance are improved [41-43]. The oxidation behavior of these intermetallics will be discussed later.

2.3 Oxidation of Niobium

Since the 1950's there have been numerous investigations of the oxidation of pure niobium. The oxidation behavior of niobium is complex because it forms several polymorphic oxides. Some of the oxides that have been observed are NbO, NbO_2 and several forms of Nb_2O_5. The principal oxide is porous Nb_2O_5, which is non volatile at ~1373°C, melts around 1440°C and tends to break during cooling [16, 24].

The oxidation of niobium above 650°C can be described as follows: It starts with a protective oxidation stage (induction period) followed by oxide spallation caused by the formation of Nb_2O_5 at prolonged time exposures. The induction period, which decreases with increasing temperature, exhibits a slow oxidation. This behavior is attributed to the adsorption and dissolution of oxygen by the niobium. NbO and NbO_2 are forming from the solid solution formed by the niobium and oxygen. After this stage, accelerated oxidation is observed created by the transformation of NbO/NbO_2 to Nb_2O_5 [24]. Hurlen [44] performed an extensive study of the reaction of niobium with oxygen at different pressures and temperatures from 150-1000°C. It was stated that the sequential stages in the oxidation of Nb were: linear (I), parabolic (II), a rate-increasing transition, linear (III), parabolic (IV) and parabolic (V).

Arbuzov et al. [45] observed structural transformations in Nb_2O_5 at different ranges of temperature. A α→β transition in Nb_2O_5 was reported. Alpha-niobium pentoxide (α-Nb_2O_5) was present at a temperature range from 500-800°C and β-Nb_2O_5 formed from 900-1000°C. Both oxides exhibited an orthorhombic crystal structure with different lattice constants. It was also observed that single crystals of β-Nb_2O_5 grow as whiskers, and these become less in number but longer as temperature is increased. Khanna [16] explained that a transition from γ→α occurs in Nb_2O_5 at 800-850°C and the whisker growth is attributed to the growth of single crystal α-Nb_2O_5. Goldschmidt [46] investigated the polymorphic forms of Nb_2O_5 and reported two types of niobium oxide: a low temperature α-Nb_2O_5 and a high temperature β-Nb_2O_5. Alpha-niobium pentoxide is metastable and transforms suddenly to β-Nb_2O_5. This oxide exhibits an orthorhombic

crystal structure. Beta-niobium pentoxide has a monoclinic structure and it is the stable between 600°C and 1230°C.

2.4 Oxidation of Refractory metal-silicide alloys

The addition of silicon and chromium to niobium, as previously mentioned, creates intermetallics and these improve the oxidation of monolithic niobium at high temperatures. Extensive oxidation studies have been performed to improve the oxidation of niobium by trying to develop protective layers of oxides [1-15, 21, 22]. Y. Murayama et al. [47] showed that the oxidation of three-phase (Nb_{ss}+Nb_3Al+Nb_5Si_3) alloys from the Nb-Si-Al-Ti system was greatly improved by the addition of Ti at 1300°C.

J. Geng et al. [3] studied the oxidation behavior at 800 and 1200°C of several niobium-silicide based alloys with modifiers. The base composition of these alloys consisted of Nb-18Si-5Cr-5Al with additional amounts of molybdenum, titanium and hafnium. The authors reported that the oxidation resistance of the base alloy was significantly improved at 800°C by the addition of titanium and the decrease in amount of molybdenum present (from 5 to 2 at %) in the alloy. Oxidation at 1200°C resulted in the spallation of oxide scales in alloys with titanium, low molybdenum and hafnium additions; titanium oxides ($TiNbO_4$, $TiNb_2O_7$ and $Ti_2Nb_{10}O_{29}$) and SiO_2 were present in the oxide scales. No protective oxide scale was observed by the authors at 800 and 1200°C. On the other hand, pesting oxidation occurred in some alloys at 800°C temperature. Pesting oxidation is observed at intermediate temperatures and it preferentially attacks the intermetallic compounds. Pesting is characterized by the disintegration of alloys into small oxide particles and powder [48]. Zelenistas [6] stated

that even though $NbCr_2$ Laves phase was stabilized by silicon in the Nb-Si-Ti system it did not prevent the alloys from pesting oxidation at 800°C. Several authors have reported the pesting phenomenon at temperatures from 700-900°C [3, 6, 8, 49].

Chan [12] studied the cyclic oxidation of niobium alloys with titanium, chromium, silicon, hafnium and germanium additions from 900-1400°C. It was found that the oxidation products for alloys was a mixture of $CrNbO_4$, Nb_2O_5, $TiNb_{10}O_{29}$ and $Nb_2O_5{\cdot}TiO_2$ and small amounts of SiO_2 and GeO_2. The best oxidation resistance was exhibited by the alloy (35.8Nb-22.5Ti-4Hf-15.6Cr-17.3Si-4.8Ge at.%), which contains higher concentrations of Laves phase $NbCr_2$ and niobium silicides than the other alloys and little amount of niobium solid solution. Even though the formation of protective oxide was not observed, the oxidation resistance of the alloys was attributed to the chromium, which promoted the formation of ternary oxide $CrNbO_4$.

Moreover, several studies have been performed on the oxidation behavior of alloys from the Nb-W-Cr with carbon modifiers. Carbon addition to the alloy with low chromium content, 5 at.% has been shown to improve its oxidation resistance. However, carbon is detrimental to the oxidation resistance of alloy with higher chromium concentration (10 at.% Cr). Also, It is been stated that there is a relationship between phase transformation and oxidation resistance for alloys with 5 and 10Cr additions. The 10Cr shows better oxidation behavior than 5Cr because at temperatures above 1100°C it suffers a phase transformation: from two-phase (Nb_{ss}+$NbCr_2$) it is converted to single phase (Nb_{ss}) reducing its oxidation drastically [9-11].

Some studies have shown the presence of thin protective scales, such as Al_2O_3, in niobium-based alloys. T. Murakami et al. [50, 51] observed the formation of such layer in powder compacts with an $Nb_3Si_5Al_2$ matrix (alloy Nb-47Si-20Al) in a temperature range from 1100-1300˚C. The authors concluded that the oxidation resistance was improved at those temperatures due to the formation of protective Al_2O_3. Brady et al. [13] studied the oxidation behavior of Laves phase ($NbCr_2$ and $TaCr_2$) composites at 1100℃ and it was concluded that $TaCr_2$ was better than $NbCr_2$ for high temperature applications. Laves phase formed by tantalum and chromium, $TaCr_2$, exhibited a parabolic oxidation and formation of protective Cr_2O_3 while $NbCr_2$ suffered from accelerated oxidation and oxide breakaway.

Recent studies have been focused in the oxidation of alloys from the Nb-Mo-Si, Mo-Si-B and Nb-Mo-Si-B systems. Chattopadhyay et al. [52] conducted an isothermal and non-isothermal oxidation study of hypo- and hyper-eutectic alloys from the Nb-Mo-Si system. At 800℃ hypereutectic alloys (Si content more than 17.5 at. %) were more susceptible to oxidation. At 1000 and 1150℃ a continuous layer of amorphous SiO_2 was observed in alloys with higher Mo content (more than 15 at. %) regardless of the hypo or hyper character. Nb_2O_5 and SiO_2 were observed in the oxide scales. A niobium oxide, $Nb_{12}O_{29}$, also appears in the oxide scale and the authors explained that $Nb_{12}O_{29}$ appears to be an intermediate reaction product of niobium and oxygen, caused by oxygen deficiency.

A different oxidation scenario occurs when boron is added to Mo-Si systems; the oxidation resistance is greatly improved by the boron addition [53-61]. Akinc et al. [57]

describes the oxidation behavior of alloys containing the $Mo_5Si_3B_x$ phase as follows: Initial oxidation of surface forms borosilicate glass and crystalline MoO_3. With further oxidation, MoO_3 volatilizes, viscous borosilicate flows and covers the pores left by MoO_3 and promotes a type of protective scale. Several authors [55-59] had reported the formation of borosilicate glass in the oxide scale. Liu et al. [56] reported the formation of four different oxide layers when niobium was added to the Mo-Si-B system. Alloy (31.5Nb-31.5Mo-30Si-7B) oxidized at 1200℃ showed the presence of these oxide scales. Layers located away of metal (layer 1 and 2) consisted of Nb_2O_5 crystals, borosilicate glass and large pores; the layer near metal (layer 3) consisted of molybdenum rich oxides MoO_3 and internal oxidation. Finally, the layer located at interface (layer 4) was identified as internal oxidation region with oxides and silicides. On the other hand, other authors reported the presence of MoO_2 near the alloy/oxide interface instead of MoO_3 [55] and the formation of amorphous silicon oxide matrix instead of borosilicate glass as the protective oxide [60].

CHAPTER 3

EXPERIMENTAL DETAILS

3.1 Alloy Preparation

The Nb-based alloy was prepared by Ames National Laboratory at the Iowa State University using arc melting technique in an argon atmosphere to prevent oxidation of metals. The metals used to prepare this alloy had a minimum of four nines in purity. The compositions of niobium, molybdenum, silicon, boron and chromium for this alloy are listed in table 3.1 in atomic percent. The composition of the investigated alloy was given by Naval Air Warfare Center. After casting, the sample ingots were electrically discharged machined (EDM) into 10 x 10 x 6 mm samples and then delivered for oxidation studies.

Table 3.1. Composition of alloy given in atomic percent

Niobium	Molybdenum	Silicon	Boron	Chromium
40	20	15	5	20

3.2 Sample Preparation

The received alloy and crucibles were prepared for oxidation experiments as follows:

1. Samples were polished down to a 600-grit finish to remove any initial oxide layer.
2. Square samples were electrically discharged machined (EDM) into 5 x 5 x 5 mm samples.

3. The samples were re-polished down to a 600-grit finish to remove any scratches and imperfections left by the EDM process.
4. Samples were measured using a micrometer and finally they underwent an ultrasonic bath for 10-15 minutes in ethanol to remove any debris or contaminants.
5. Caps were made out of Leco 528 HP crucibles in order to prevent any material loss during the oxidation process.
6. Leco 528 HP crucibles and caps were furnace dried at 300℃ for 2 hrs previous to oxidation.

3.3 Sample Oxidation

The alloy was subjected to oxidation in air using box furnaces over a temperature range from 700-1300℃. A furnace (Linderberg/Blue M model 1100) was used for experiments performed at 700-900℃, and a computer-controlled high temperature furnace (Sentro Tech. Corp model ST-1600-888) was used from 1000-1300℃. The ramp time for both furnaces was set to 10˚C per minute. Two oxidation studies were performed in this alloy: short term oxidation (STO) and long term oxidation (LTO). STO consisted of one cycle of 24 hr., while LTO consisted of seven cycles of 24 hours giving a total exposure time of 168 hr. After each cycle, samples were furnace cooled to room temperature. Initial weight and final weight after each cycle was recorded using a Sartorius Analytical balance (model MC210S) with precision up to six decimal places. Weight gain/loss per unit area recorded for each sample indicates the amount of oxidation at a given temperature.

3.4 Sample Characterization

After the oxidation was completed, oxidized samples were stored in glass vials waiting for sample characterization. Sample characterization for as cast alloy and oxidized samples consisted of optical microscopy (OM), scanning electron microscopy (SEM), which includes energy dispersive spectroscopy (EDS) and x-ray mapping, and x-ray diffraction (XRD). Sample characterization was performed in facilities provided by the University of Texas at El Paso.

3.4.1 Optical Microscopy OM

Samples (as cast and oxidized) for OM were ground through a series of silicon carbide papers: 240, 400, 600, 800, 1000 and 1200. Final polishing was performed only in as cast samples with a series of 1μm, 0.3μm and 0.5μm alumina slurries and a felt cloth. Samples were rinsed in water and dried using ethyl alcohol. Sample etching was carried out by swabbing sample for 2 to 10 s using ASTM 66 etchant: 6mL hydrofluoric acid (HF), 3mL nitric acid (HNO_3) and 6mL hydrochloric acid (HCL). An optical microscope (Reichert MEF4 A/M) equipped with a digital camera (DCM500) and Scope Photo Software 3.0 was utilized to obtain micrographs of alloy and oxidized samples.

3.4.2 Scanning Electron Microscopy, SEM

Samples for SEM analysis were sputter coated with gold using a SPI-MODULE sputter coater to prevent charging effects. All SEM studies were performed on a Hitachi S-4800 Scanning Electron Microscope equipped with EDS and BSE (Back Scatter Electron) detectors. Sample characterization included BSE imaging, EDS analysis and

x-ray mapping. BSE imaging was used to identify the different phases present in the microstructure and in the oxide scale. EDS analysis was performed in the base metal and in the oxide scale; at least five readings were taken for each phase and the average of these was reported. The elapsed live time for each reading was set to 30-50 seconds. Calibration of EDAX detector was performed periodically to ensure proper readings. The ratio of readings gave us an estimated oxide and phase stoichiometry, which was confirmed by XRD technique. X-ray mapping was performed to locate the elements present in the alloy. To obtain contrast between element maps the dwell time was set to 15-18 seconds, which gave a mapping time of 13-16 minutes. All SEM and EDS characterization was performed at an accelerating voltage of 20kV, probe current of 20μA and a working distance from 12.0-15.5 mm.

3.4.3 X-Ray Diffraction, XRD

A Sintag XDS 200 x-ray diffractometer with monochromatic CuKα radiation (λ=1.54056Å), voltage of 45kV and current of 45mA was used to characterize the phases present in the as received alloy and the oxides formed in the oxide scale at various temperatures. The parameters used for XRD diffraction analyses are shown in table 3.2.

Table 3.2. Parameters used for XRD diffraction analysis

Generator voltage	45kV
Generator current	40 mA
Step size	0.3 s
Start angle	5˚
Stop angle	90˚
Preset time	0.5 s
Tube divergence slit	2
Tube scatter slit	4
Detector divergence slit	0.1
Detector receiving slit	1

Sample preparation for XRD analysis was done by pulverizing oxidation products until a fine powder was obtained. The powder was adhered to a glass slide by using petroleum jelly. Once a pattern was obtained, the most intense peaks were matched to the oxides using powder diffraction files PDF from a Powder Diffraction Database. As received alloy analysis was performed using the same procedure mentioned above but it was not converted into powder.

3.4.3 Phase Diagram Modeling

A phase diagram calculation software for multicomponent systems Pandat™8.1 provided by CompuTherm LLC (Madison, WI) was used to calculate the isothermal sections of the alloy at various temperatures. This software predicts the phases present in the alloy based on the crystal structures and amount of alloying elements. The stability of these phases is calculated based on thermodynamic data.

CHAPTER 4

RESULTS AND DISCUSSION

4.1 As Cast Characterization

4.1.1 Scanning Electron Microscopy, SEM

A backscatter (BSE) image of the as cast or as received microstructure of Nb-20Mo-15Si-5B-20Cr alloy is shown in Figure 4.1(a); contrast indicates the different phases present in the alloy. The alloy consisted of four phases, solid solution (α), silicides Nb_5Si_3, Nb_3Si and Laves phase $NbCr_2$. White areas represent the solid solution (α) of Nb and Mo. Light gray areas represent a mixture of silicides Nb_3Si and Nb_5Si_3, while dark gray areas are $NbCr_2$. Also, the alloy contained a eutectic like microconstituent showing α, Nb_3Si and $NbCr_2$. Figure 4.1(b) shows a high magnification (3500x) image of the eutectic like region where again white areas are (α), light gray areas correspond to silicide, Nb_3Si, and dark gray areas are $NbCr_2$. Boron was added to the alloy as a phase stabilizer. However, the characterization techniques used in this investigation, such as XRD, SEM and EDS analysis could not detect the presence of boron in the alloy. Therefore, the effect of boron addition in the as received microstructure of the alloy and in its oxidation behavior will not be discussed. Other characterization techniques, such as wave dispersive spectrometry (WDS) also called electron probe microanalysis (EPMA) or EDS analysis with boron detection capabilities are recommended to study the boron effect. Figure 4.2 shows the elemental x-ray mapping of the alloy. The concentration or contrast of elements is related to the phases that are forming. X-ray mapping of elements shows that chromium is highly concentrated in the Laves phase $NbCr_2$ with significant amounts of silicon. Little chromium concentration is

observed in the α phase as well as in the silicide Nb_5Si_3, but higher chromium concentration is shown in eutectic Nb_3Si. As expected, silicon is mostly concentrated in silicides and little concentration of this element is found in the α phase. Molybdenum is mostly located in the α phase. Table 4.1 shows the elemental analysis performed in each phase. It can be observed that chromium concentration in the α phase and Nb_5Si_3, 9.91 and 2.34 at% respectively, is lower than in the eutectic like microconstituent. Chromium concentration in the eutectic α phase and Nb_3Si is 17.25 and 9.83 at%, respectively. Also, silicon concentration increases in the eutectic α and Laves phase $NbCr_2$ exhibits a silicon concentration of 15.65 at%.

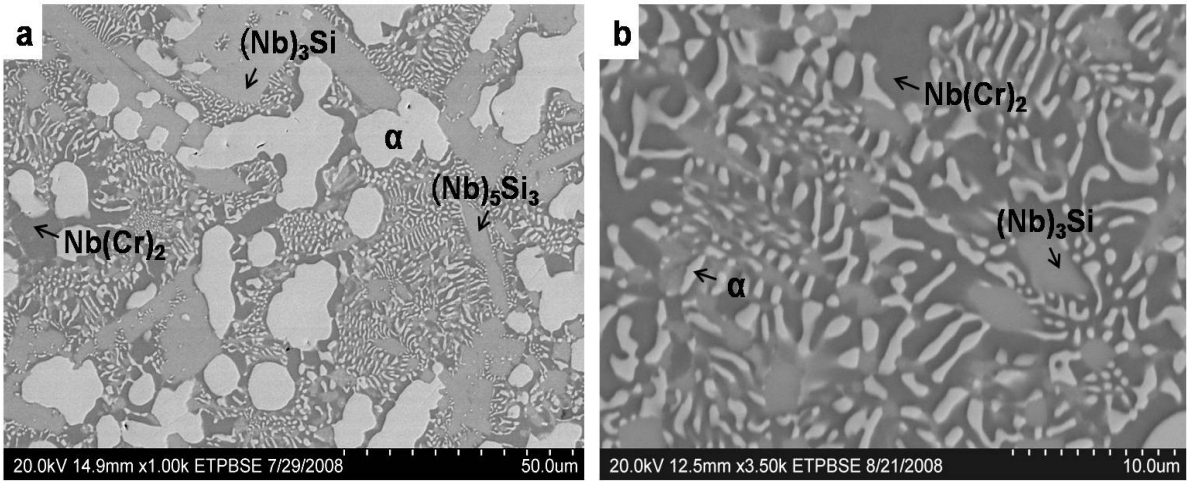

Figure 4.1. BSE micrographs of as cast alloy: Microstructure consists of solid solution α (white area), Nb_3Si and Nb_5Si_3 (light gray areas), $NbCr_2$ (dark gray areas) and eutectic like microconstituent formed by α, Nb_3Si and $NbCr_2$. (b) shows a magnified view of eutectic microconstituent.

Table 4.1. Elemental analysis of phases present in as cast alloy

Element	Phases				
	Solid solution	Silicide	Eutectic		
	α (at.%)	$(Nb)_5Si_3$ (at.%)	α (at.%)	$(Nb_3)Si$ (at.%)	$Nb(Cr)_2$ (at.%)
Si	2.93	31.60	5.72	22.35	15.65
Nb	48.15	55.52	44.58	37.25	31.68
Mo	39.01	10.54	32.45	17.02	12.04
Cr	9.91	2.34	17.25	9.83	40.63

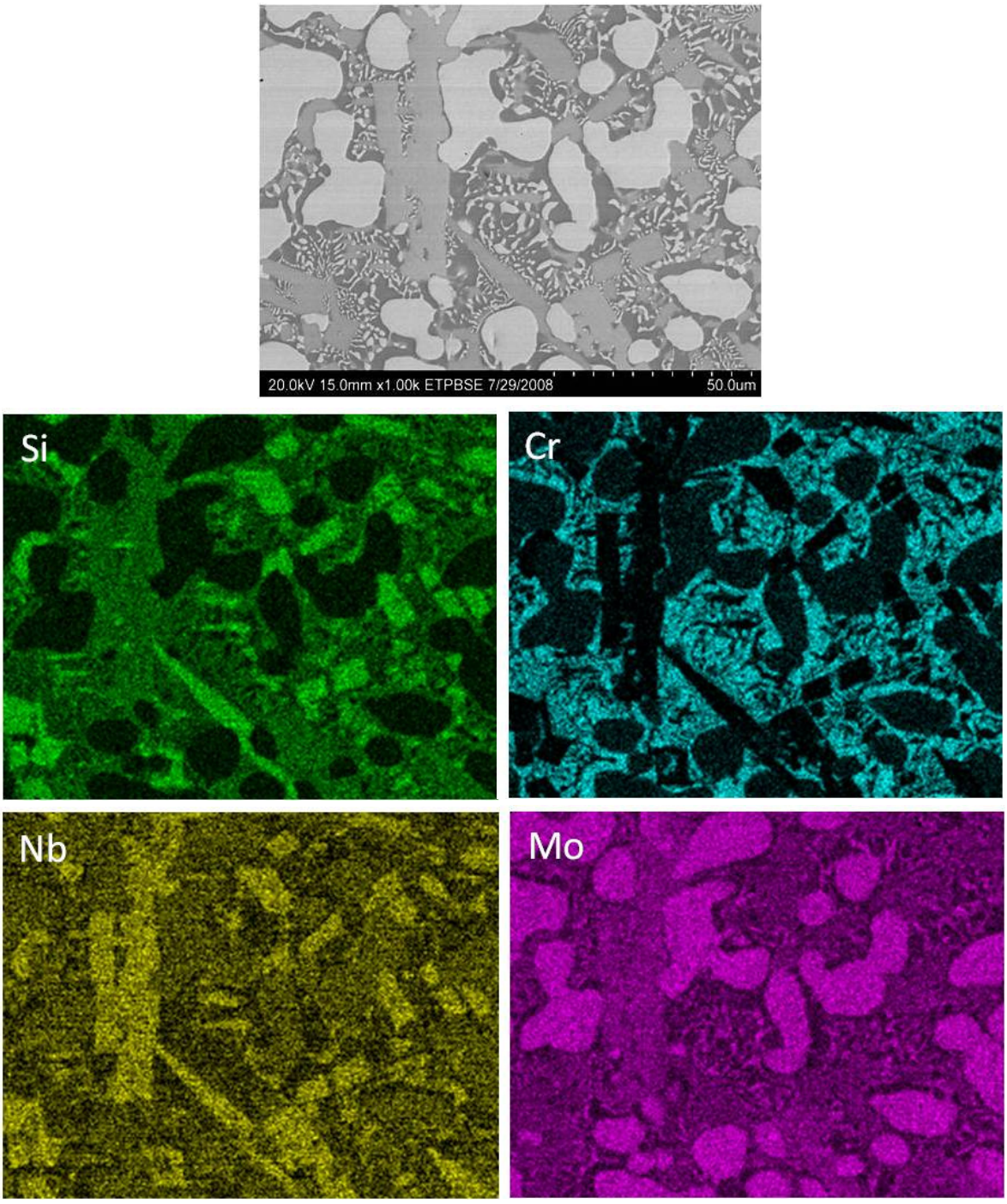

Figure 4.2. Elemental x-ray mapping of Si, Cr, Nb and Mo performed on the as cast microstructure. High concentration or contrast of elements is related to the phases that are forming.

4.1.2 X-Ray Diffraction, XRD

The XRD pattern obtained for the as cast alloy is shown in Figure 4.3. Individual phases and their crystal structures were identified by matching the characteristic XRD peaks against powder diffraction files. The presence of four phases was confirmed by this characterization technique, body centered cubic BCC solid solution (α), tetragonal Nb_5Si_3, tetragonal Nb_3Si and hexagonal Laves phase $NbCr_2$. The solid solution (α) is rich in Nb and Mo and a BCC structure was observed since both Nb and Mo possess this crystal structure. The Laves phase $NbCr_2$ found in the alloy corresponds to the high temperature hexagonal structure (C14), which was stabilized by the presence of Si.

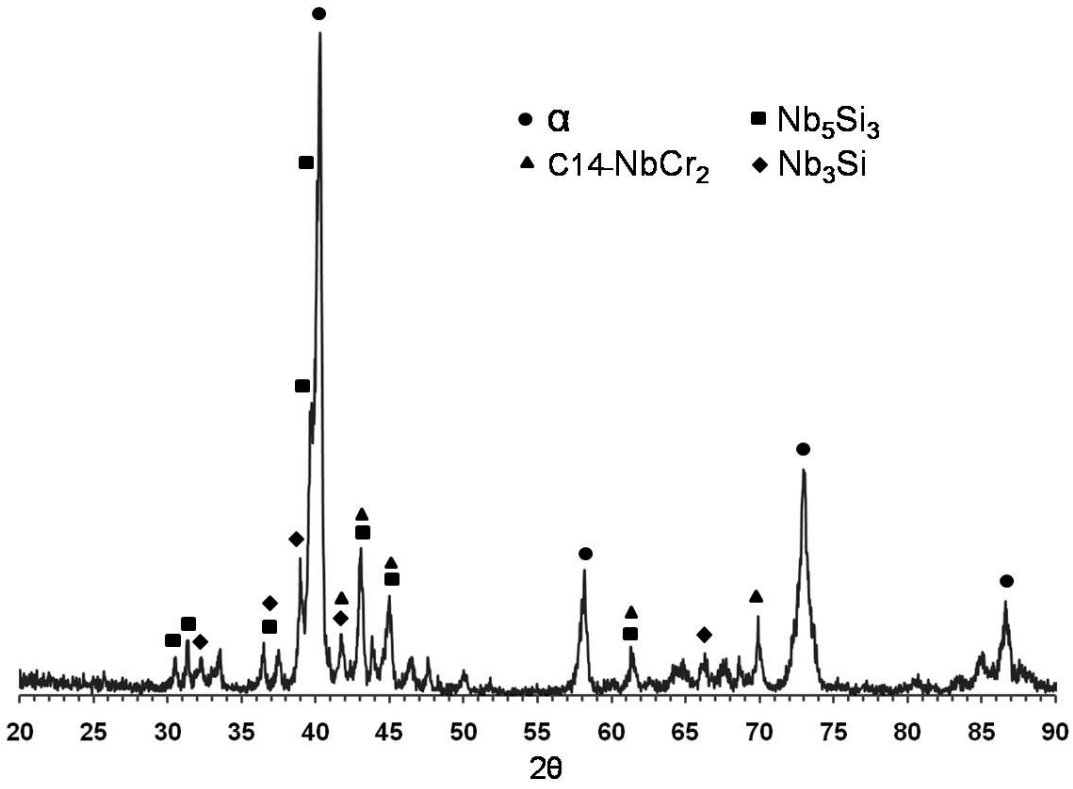

Figure 4.3. XRD pattern of the as cast alloy.

4.1.3 Phase Diagram Modeling

The calculated isothermal sections at 800°C, 1000°C, 1200°C and 1300°C from the Nb-Mo-Si-Cr system are presented in Figure 4.4. The isothermal sections were modeled by using Pandat^{TM} 8.1 software, which calculates the phase stability based on the most recent thermodynamic data.

The quaternary isothermal sections were calculated by fixing the amount of chromium at 20 percent and setting the amounts of niobium, molybdenum and silicon at 80 percent. The alloy's composition was set to 45Nb-20Mo-15Si-20Cr. Boron was not included in the software's database. The software predicted the phases found in the alloy, which are, the solid solution (α), Nb_5Si_3 and $NbCr_2$. The presence of Nb_3Si was not observed in the calculated isotherms. However, the software confirmed the presence of the hexagonal C-14 Laves phase $NbCr_2$. It can be observed that the phases present in the alloy remained stable at all temperatures and the alloy remained in the four-phase region.

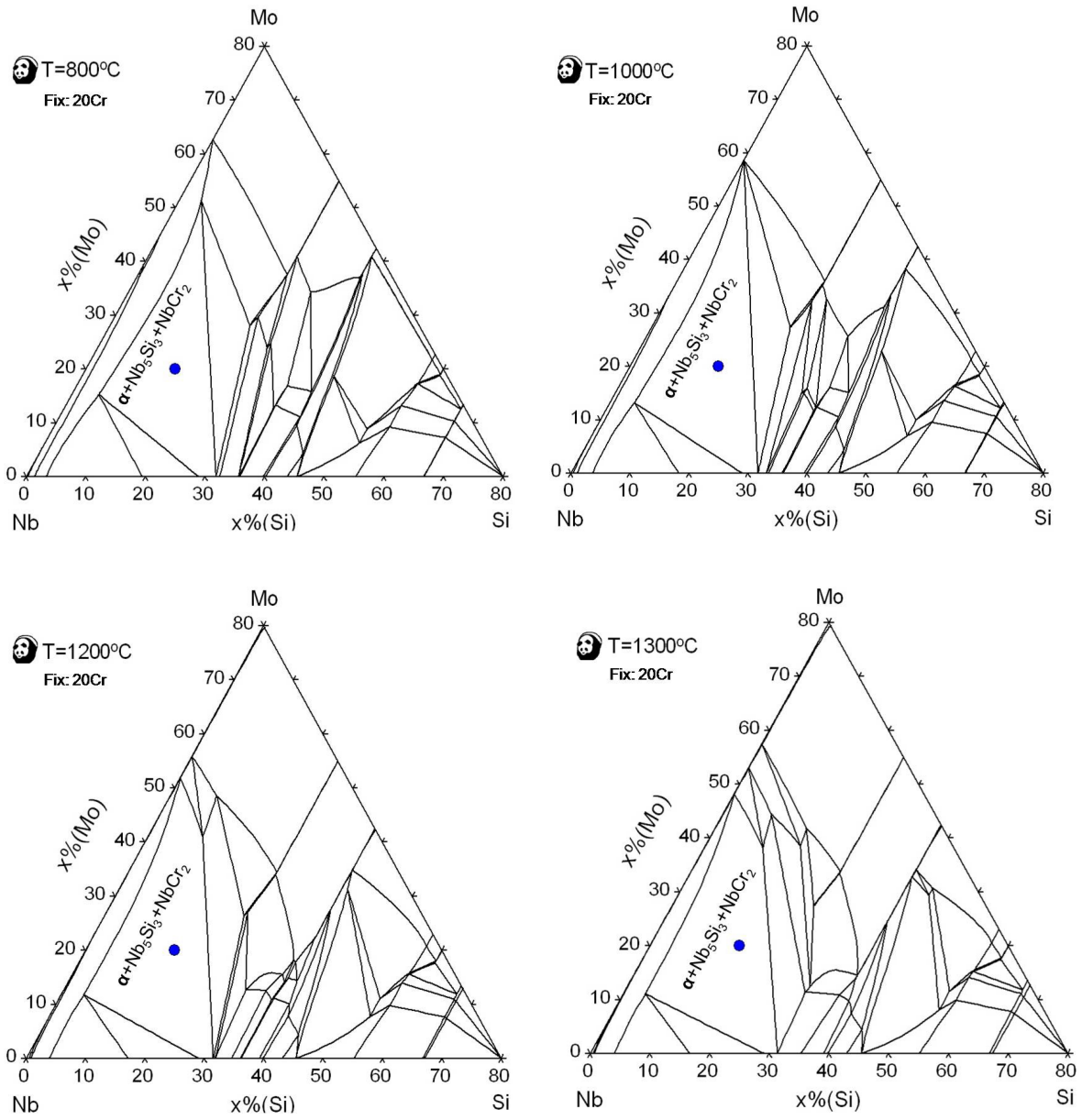

Figure 4.4. Isothermal sections calculated at 800℃, 1000℃, 1200℃ and 1300℃ for the Nb-Mo-Si-Cr system.

4.2 Short Term Oxidation, STO

The short term oxidation curve, obtained after 24 hours of exposure in air for a temperature range from 700-1400°C, is shown in Figure 4.5. This curve was calculated by plotting the mass gain per unit area as a function of oxidation temperature. The oxidation behavior of the alloy can be described in stages. The first stage occurs at 700°C, this stage is characterized by an increase in mass gain per unit area. The second stage occurs at 800°C, and a decrease in mass gain can be observed. The oxidation products at these two stages consist of a small amount of loose powder and a thin oxide layer surrounded the metal. The third stage shows better oxidation resistance than stage one and occurs at 900 and 1000°C. This stage shows the least weight gain by the alloy. Oxidation products for this stage are thin layers of oxide surrounding the metal with no loose oxide. The fourth stage occurs at temperatures from 1100-1300°C and the mass gain per unit area at that temperature was constant. Spallation of oxides was observed at 1100°C and a thick bulky oxide layer surrounded the metal at 1100, 1200 and 1300°C. The fifth and final stage occurred at 1400°C; at this temperature the metal was completely transformed into a swollen bulky oxide. The most weight gain per unit area was observed at this temperature.

According to the oxidation behavior observed at different temperatures and the stages identified, detailed short term oxidation experiments at 800, 1000, 1200 and 1300°C were conducted to determine the oxidation kinetics at 24 hours of exposure. This study was performed by periodic removal of a specimen, weighing and re-insertion for further exposure at constant temperature. The alloys were oxidized up to 24 hours

in six cycles of 2, 3, 4, 5 and 10 hours and cooled inside the furnace to room temperature. Figure 4.6 shows the short oxidation curve obtained by plotting the mass gain per unit area as a function of oxidation time. The oxidation kinetics of the alloy follows a parabolic behavior at all temperatures (800, 1000, 1200 and 1300℃.) The parabolic oxidation rate constants (k_p) were calculated by the least-square method, linear-regression analysis of the mass gain data and the equation

$$\left(\frac{\Delta m}{A}\right)^2 = k_p t \tag{4.1}$$

where, ∆m is the mass change of the specimen, A is the surface area and t is the exposure time. Table 4.2 shows the calculated parabolic oxidation rate constants and the mass gain per unit area at 24 hours of exposure at each temperature. The oxidation rate constant determines the rate of material consumption. From Figure 4.6, it can be observed that the mass gain and the oxidation rate are proportional to the oxidation temperature. The highest oxidation rate and mass gain was observed in the alloy oxidized at 1300℃. The values for oxidation rate constant and mass gain per unit area at 1300℃ are 143.7 $mg^2/cm^4/hr$ and 57.07 mg/cm^2 respectively. The alloy exhibited better oxidation resistance at 800℃ with an oxidation rate constant of 4.84 $mg^2/cm^4/hr$ and a mass gain per unit area of 11.4 mg/cm^2. Oxidation product at 800℃ consisted of loose powder and thin oxide scale and metal. The spallation of oxides was observed at 1000, 1200 and 1300℃.

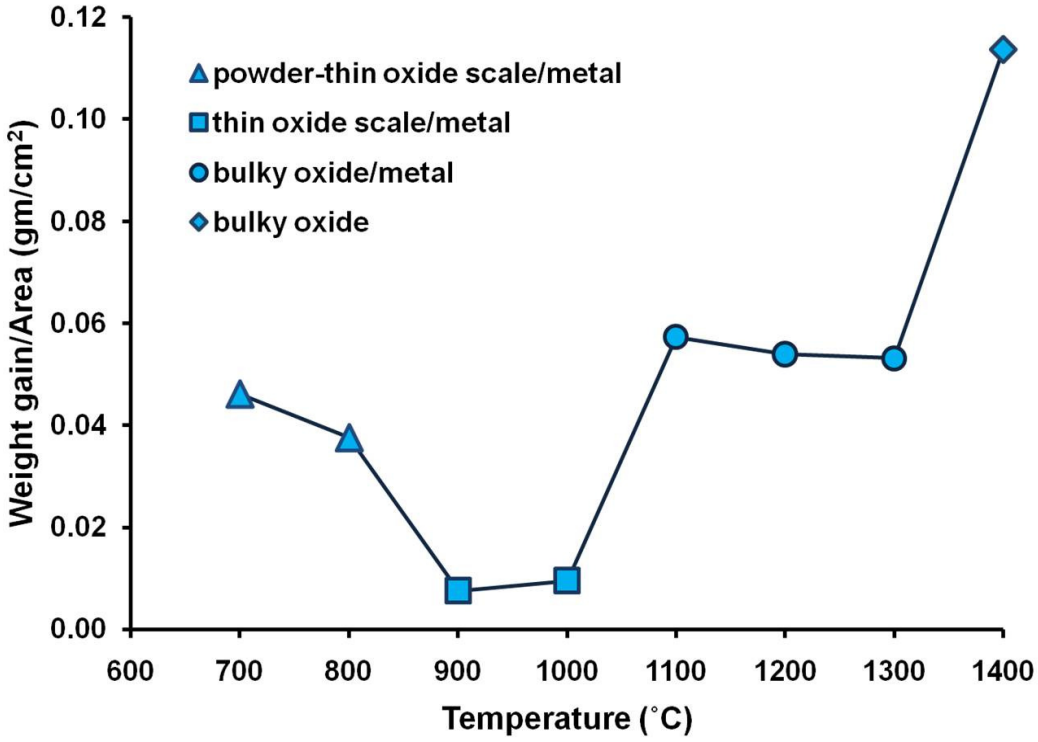

Figure 4.5. Short term oxidation curve (weight gain per unit area vs. oxidation temperature) obtained after 24 hours of exposure in air. Curve indicates oxidation products final state (▲ powder-thin oxide scale/metal, ■ thin oxide scale/metal, ● bulky oxide/metal and ◆ bulky oxide.)

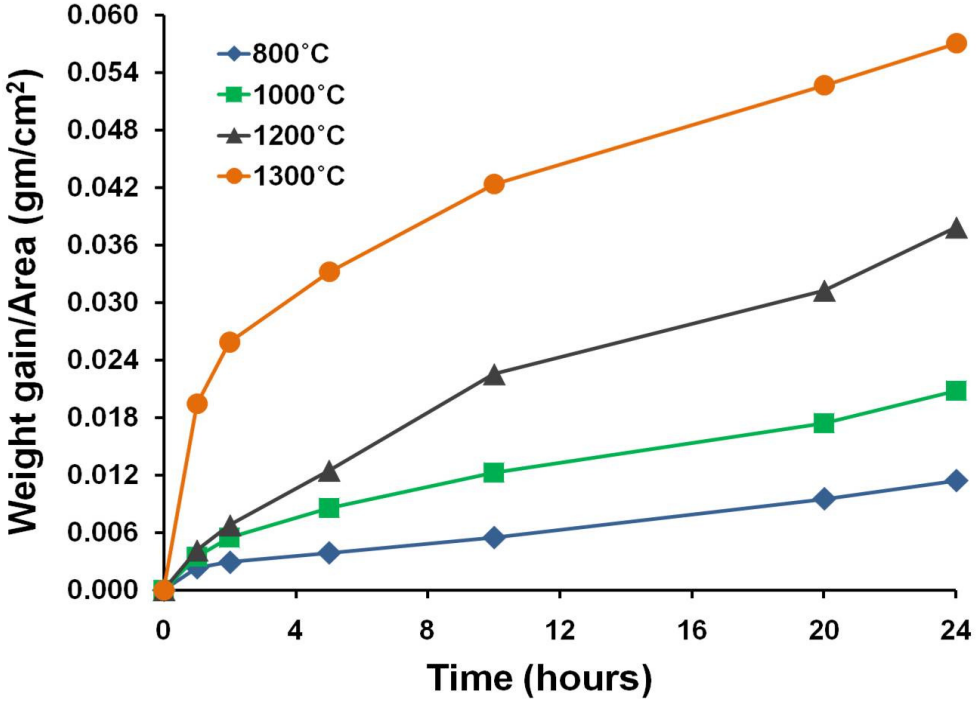

Figure 4.6. Short term oxidation curve (weigh gain per unit area vs. oxidation time) obtained after 24 hours of exposure in air. Oxidation at all temperatures followed a parabolic behavior.

Table 4.2. Oxidation rate constants and mass gained after 24 hours of exposure at 800, 1000, 1200 and1300°C.

Temperature (C°)	Total mass gain per area	Oxidation rate constant		R^2
	$\Delta m/A$ (mg/cm^2)	k_l (mg/cm^2/hr)	k_p (mg^2/cm^4/hr)	
800	11.4	-	4.84	0.957
1000	20.8	-	16.64	0.986
1200	37.8	-	54.15	0.974
1300	57.07	-	143.7	0.943

4.2.1 Characterization of Short Term Oxidation Products

4.2.1.1 Scanning Electron Microscopy, SEM

Figure 4.7 shows BSE micrographs of the oxide-metal interfaces formed on alloy after 24 hours of exposure at 700-1200°C. Oxidation scales formed at 700 and 800°C, Figures 4.7(a) and (b) respectively, show a highly porous oxide scale with dense mixture of oxides. Light gray oxides observed at 700°C, Figure 4.7(a), consist of a mixture of Nb_2O_5 and MoO_3, while dark gray areas represent a mixture of SiO_2, $CrNbO_4$ and Cr_2O_3. Oxide scale formed at 800°C, Figure 4.7(b), was composed of Nb_2O_5 (light gray areas) and $CrNbO_4$ (dark gray areas.) Figure 4.7(c) shows the oxide scale formed at 900°C. It can be observed that the oxide scale was less porous than at lower temperatures. Dense light gray areas were composed of Nb_2O_5, while dark gray areas are a mixture of SiO_2 and $CrNbO_4$. A porous gray oxide was also observed, which corresponds to $CrMoO_4$. Oxide scales formed at 1000-1200°C, Figures 4.7(d-f), were similar. Scales were composed of fine oxide particles and porous oxides. A mixture of $CrMoO_4$ and SiO_2 was observed in oxide scales formed at 1000°C and 1100°C, Figures 4.7(d) and (e) respectively. $CrNbO_4$ is located at the oxide-metal interface in alloy oxidized at 1000°C. At 1100°C, a layer of SiO_2 and Nb_2O_5 (dark gray areas) also

appears at the interface and a mixture of Cr_2O_3, SiO_2 and Nb_2O_5 conforms the oxide scale. Figure 4.7(f) shows the oxide-metal interface of alloy oxidized at 1200℃. The oxide scale was composed of Nb_2O_5, $CrNbO_4$ and MoO_3.

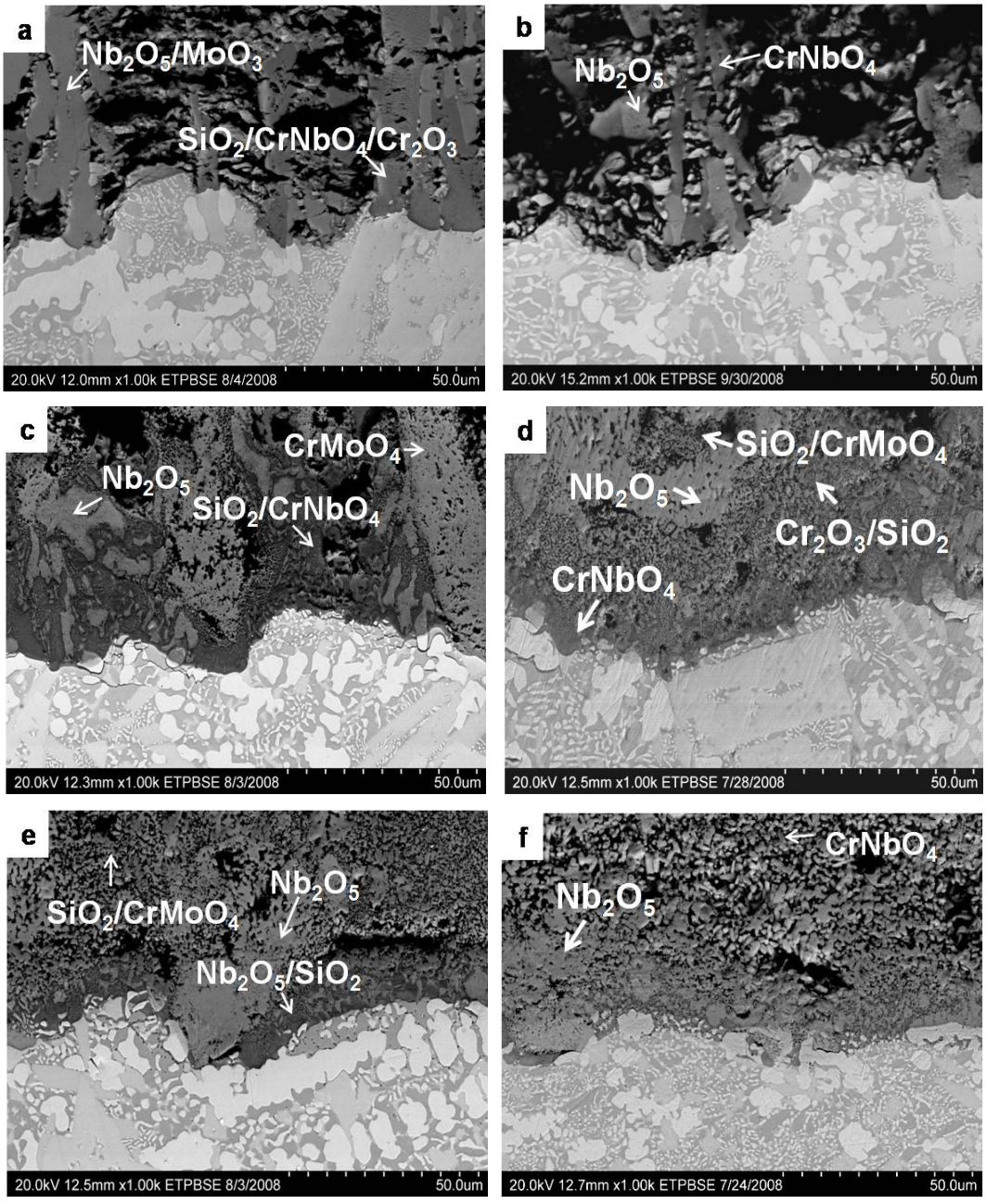

Figure 4.7. BSE micrographs of the oxide-metal interfaces formed on alloy oxidized for 24 hours of exposure at (a) 700℃, (b) 800℃, (c) 900℃, (d) 1000℃, (f) 1100℃ and (d) 1200℃. Nb_2O5, $CrNbO_4$ and SiO_2 were the common oxides present at all temperatures.

SEM analysis of the oxide scale formed at 1300℃ showed that the scale is composed of three layers. Figure 4.9 (a) shows an overall view of the oxidized specimen and the oxide layers formed. Magnification of micrograph is 300x. Figure 4.9 (b) shows a high magnification (1000x) micrograph of the oxide-metal interface and the first oxide formed in contact with the metal. This oxide layer (layer 1) consists of a mixture of Nb and Mo rich oxides. Elemental analysis on these oxides revealed the presence of MoO_2 and MoO_3 (light gray areas) and Nb_2O_5 (gray areas). SiO_2 (dark gray areas) was observed as a thin layer located at the interface; however this oxide layer was not continuously formed. The layer 2; shown in Figure 4.9(c), consists of globular particles of $CrNbO_4$ (gray areas) oxide embedded in a SiO_2 matrix (black areas). Figure 4.9 (d) illustrate the outermost layer (layer 3) formed in oxidized alloy. This layer is mainly composed of elongated Nb_2O_5 particles (white areas) with some regions or spots of $CrNbO_4$ (gray areas) embedded in a SiO_2 matrix (black areas). The SiO_2 matrix was only found in oxide layers formed at 1300 and 1400℃. Sample oxidized at 1400℃ was completely transformed into a swollen oxide. Figure 4.11(a) shows a low magnification (300x) BSE image of the oxide formed at 1400℃. Figure 4.11(b) shows a detailed view of sample. Magnification of micrograph is 500x. The oxide microstructure consisted of elongated Nb_2O_5 particles (white areas), globular $CrNbO_4$ particles (gray areas) embedded in a SiO_2 matrix (dark areas).

Table 4.3 shows the composition of oxides obtained from the elemental analysis performed on oxide scales. The elemental analysis made possible the location of oxides. The presence of these oxides was later confirmed by XRD.

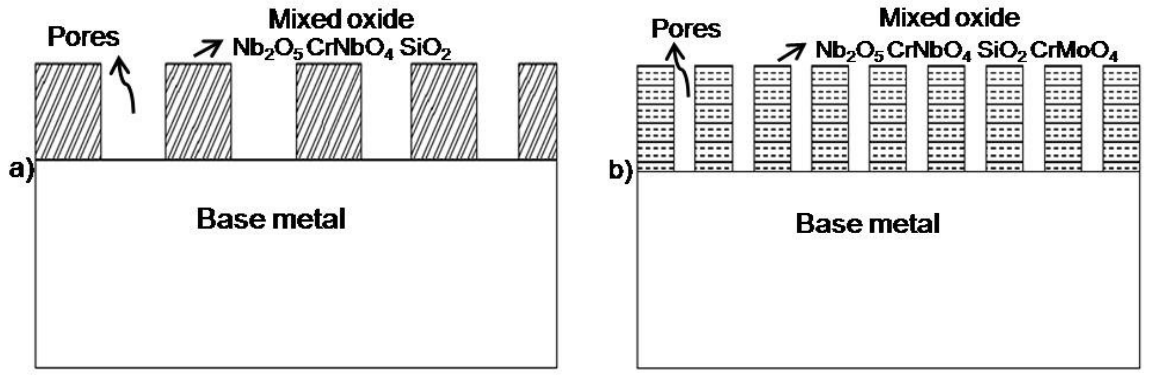

Figure 4.8. A schematic representation for oxide layer formed in samples oxidized at a) 700-800℃ and b) 900-1200℃ after 24 hours of exposure. Oxide layer formed at 900-1200℃ was less porous than at lower temperatures.

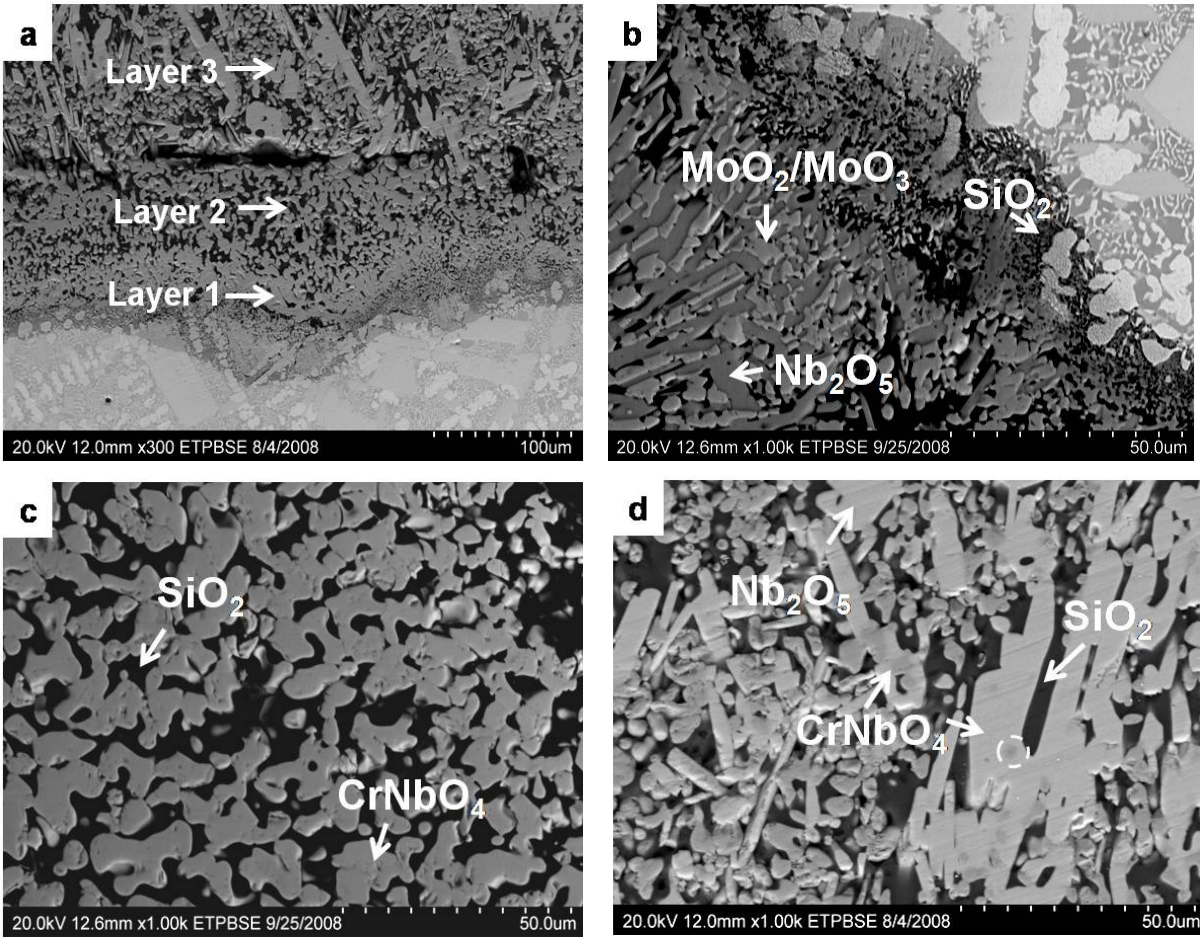

Figure 4.9. BSE micrographs of alloy oxidized at 1300℃ for 24 hrs: (a) shows on overall view of the oxidized sample and the distinct oxide layers, (b) illustrates the oxide-metal and first oxide layer in contact with metal. Layer 1 consists of MoO_3, Nb_2O_5 and SiO_2, while layer 2 (c) is formed by globular particles of $CrNbO_4$ embedded in SiO_2 matrix. Layer 3 (d) shows elongated particles of Nb_2O_5 with $CrNbO_4$ regions in a SiO_2 matrix. Magnification of micrographs is (a) 300x and (b-d) 1000x.

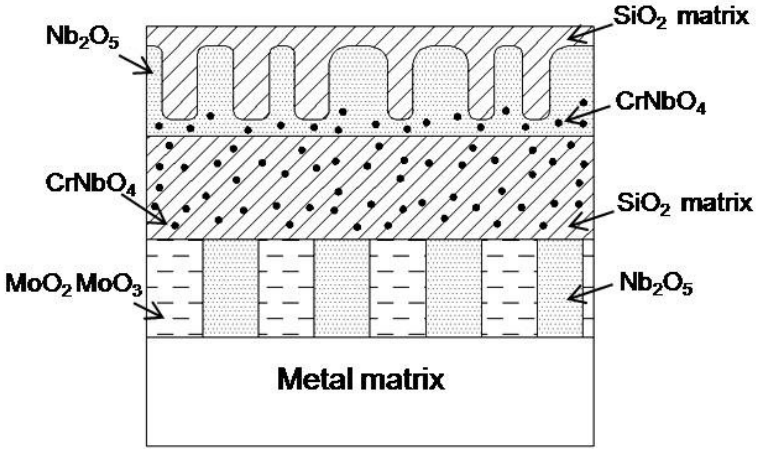

Figure 4.10. A schematic representation for the three oxide layers formed in sample oxidized at 1300℃ after 24 hours of exposure.

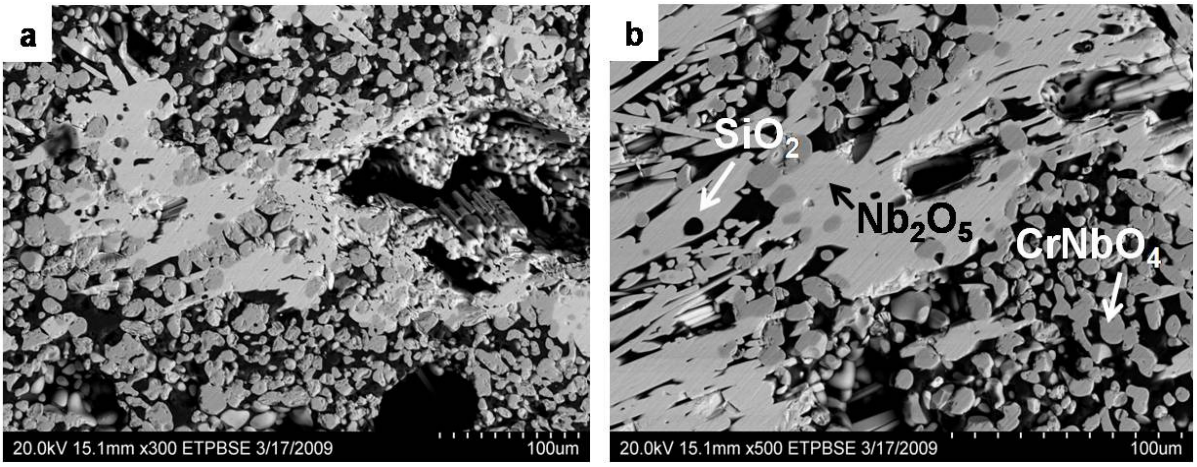

Figure 4.11. BSE micrographs of oxide formed at 1400℃ for 24 hrs: (a) shows on overall view of the oxide; oxide microstructure (b) consisted of elongated particles of Nb_2O_5 and globular particles of $CrNbO_4$ regions in a SiO_2 matrix. Alloy oxidized completely at this temperature.

Table 4.3. EDS analysis of oxide scales developed in alloy after 24 hours of oxidation at 700-1400°C.

Temperature (C°)	Oxide	O	Si	Nb	Mo	Cr
700	Nb_2O_5/MoO_3	46.12	3.07	23.89	17.81	9.11
	$Cr_2O_3/SiO_2/CrNbO_4$	39.10	11.89	22.27	11.05	15.68
800	Nb_2O_5	40.38	7.61	35.90	10.33	5.78
	$CrNbO_4$	21.88	12.52	25.88	8.99	30.73
900	$SiO_2/CrNbO_4$	46.51	11.58	22.00	4.58	15.33
	$Nb_2O_5/CrMoO_4$	47.71	2.25	33.59	8.18	8.28
	Nb_2O_5	47.01	2.74	39.33	8.42	2.51
1000	$CrNbO_4$	49.92	4.52	20.71	5.13	19.72
	$CrMoO_4/SiO_2$	52.76	15.83	21.67	4.90	4.84
	Nb_2O_5	51.06	2.93	34.77	7.85	3.39
	Cr_2O_3/SiO_2	51.05	10.19	17.75	7.00	14.02
1100	$SiO_2/CrMoO_4$	49.29	12.35	18.68	10.64	9.05
	SiO_2/Nb_2O_5	48.90	14.26	23.52	7.73	5.59
	Nb_2O_5	50.76	2.38	35.99	7.70	3.17
1200	$CrNbO_4$	43.73	4.11	23.72	4.95	23.49
	Nb_2O_5	51.36	4.88	31.45	9.59	2.72
1300 first oxide layer	MoO_2/MoO_3	44.76	<1	13.58	29.69	11.96
	Nb_2O_5	49.39	<1	40.02	10.24	<1
	SiO_2	55	31.75	4.61	5.84	2.81
1300 last oxide layer	Nb_2O_5	51.14	<1	40.98	7.88	<1
	$CrNbO_4$	50.12	<1	22.41	5.51	20.13
	SiO_2	55.57	36.52	5.75	1.71	<1
1400	Nb_2O_5	57.8	<1	35.2	6.1	<1
	$CrNbO_4$	55.02	0.51	20.54	4.93	19.01
	SiO_2	64.62	28.03	1.87	4.11	1.38

Figure 4.12 through 4.14 illustrates the elemental x-ray mapping of samples oxidized at 800, 1000 and 1300°C, respectively. Analysis was performed along the oxide-metal interface at a magnification of 1000x. Maps show the distribution of niobium, molybdenum, silicon and oxygen along the metal and oxide scale. At 800°C, Figure 4.12, oxide scale is mainly formed by niobium and molybdenum oxides. Chromium and silicon concentrations along the oxide scale were observed in localized areas. Figure 4.13 shows the maps for sample oxidized at 1000°C. At this temperature, the oxide scale is mainly composed of silicon and chromium rich oxides.

Niobium concentration was limited to some areas and low molybdenum concentration was observed. Elemental mapping at 1300°C, Figure 4.14 shows that, indeed, first oxide layer in contact with metal contains molybdenum and niobium rich oxides. Chromium concentration was low and formation of SiO_2 along the interface can be appreciated.

4.2.1.2 X-Ray Diffraction, XRD

The oxidation products in powder form were characterized by XRD. Figure 4.15 presents the XRD patterns of oxides obtained from samples oxidized at 700, 800, 1100, 1200 and 1300°C 24 hours of exposure. XRD analysis at 900 and 1000°C was not performed since insufficient oxide products were formed at those temperatures. XRD technique detected the presence of Nb_2O_5, $CrNbO_4$, Mo_4O_{11}, MoO_3, MoO_2, $CrMoO_4$ and SiO_2. The predominant oxides formed at all temperatures were tetragonal $CrNbO_4$ and monoclinic Nb_2O_5. XRD patterns were similar at all temperatures except at 700 and 800°C. An extra peak of Nb_2O_5 appeared at those temperatures at a 2θ value of 23°. Examination of pattern revealed that the reflection corresponds to the orthorhombic form of Nb_2O_5. Figure 4.16 shows the XRD patterns for samples oxidized in six cycles up to 24 hours at 800, 1000, 1200 and 1300°C. Again, the presence of $CrNbO_4$ and Nb_2O_5, MoO_3 among other oxides was confirmed. Table 4.4 summarized the oxides identified by XRD at different temperatures.

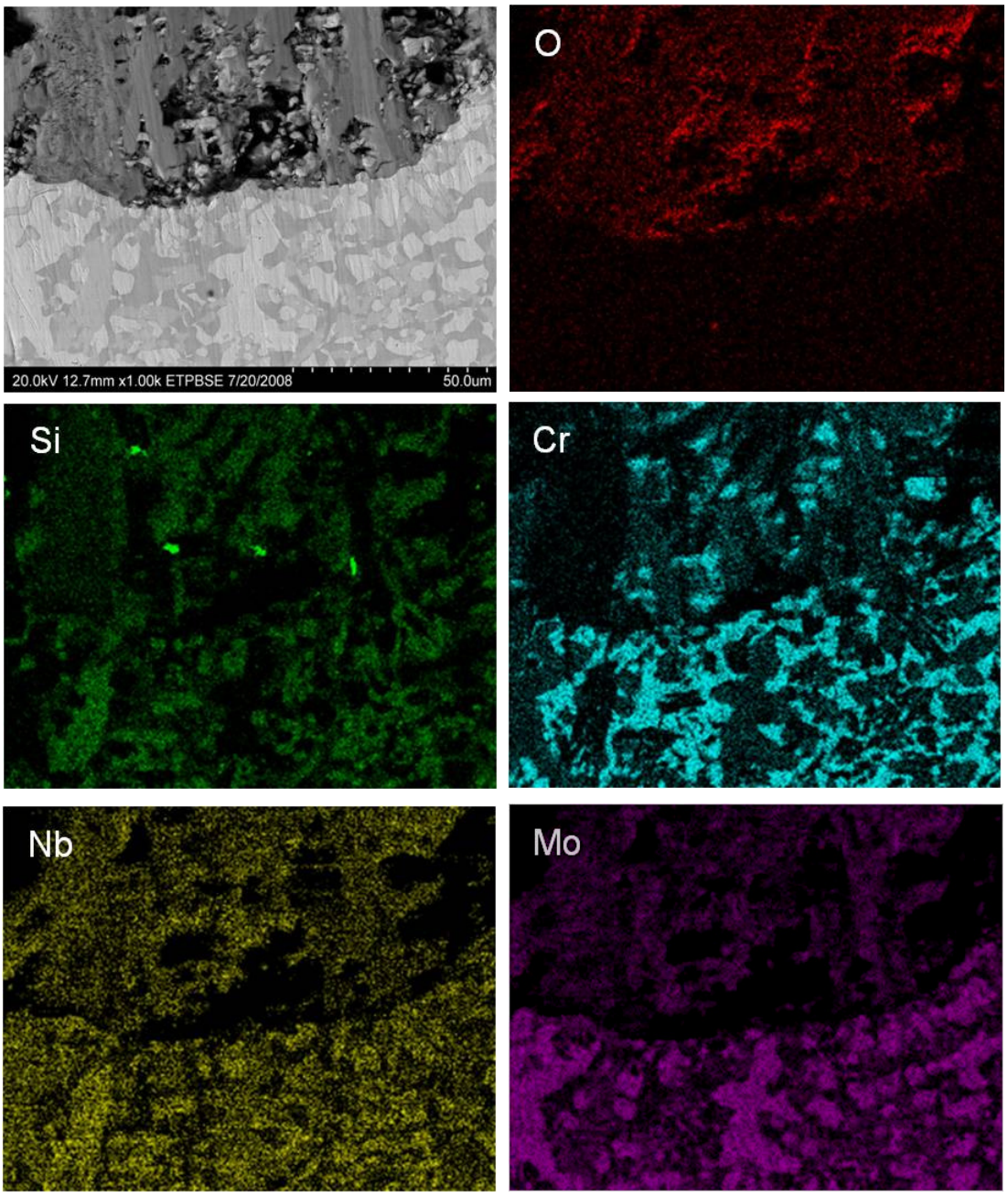

Figure 4.12. Elemental x-ray mapping of O, Si, Cr, Nb and Mo performed on the oxide-metal interface obtained at 800°C.

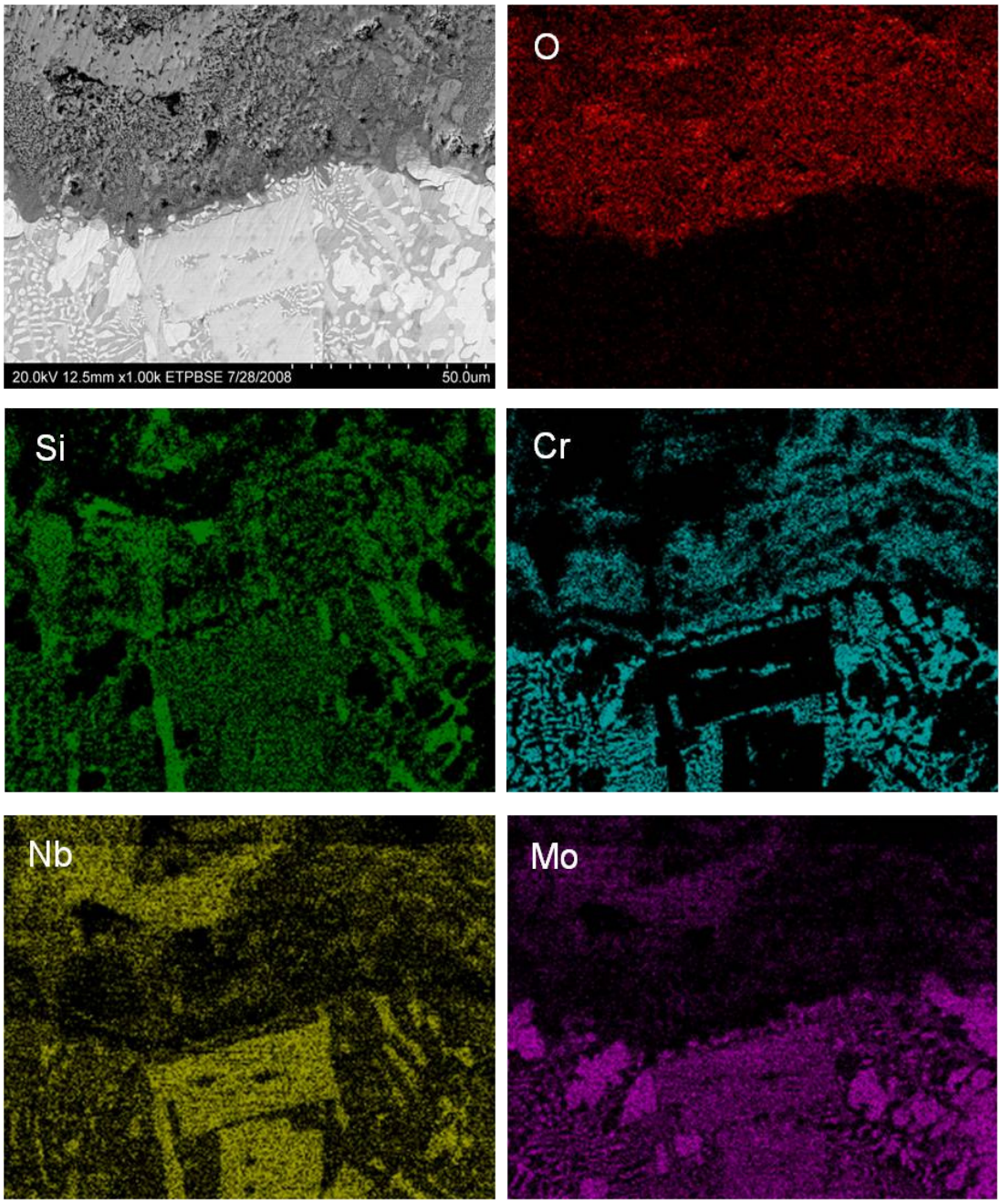

Figure 4.13. Elemental x-ray mapping of O, Si, Cr, Nb and Mo performed on the oxide-metal interface obtained at 1000℃.

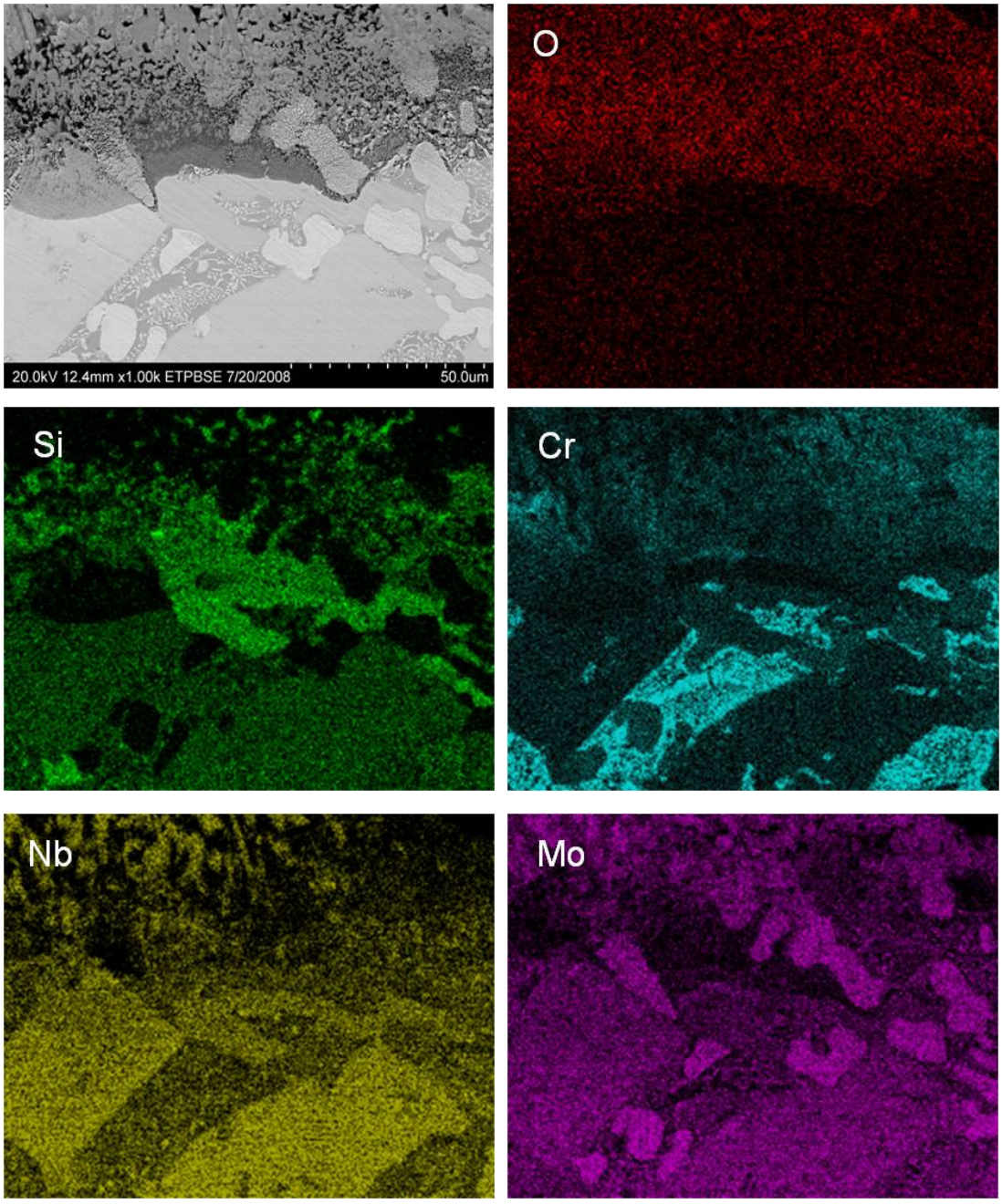

Figure 4.14. Elemental x-ray mapping of O, Si, Cr, Nb and Mo performed on the oxide-metal interface obtained at 1300℃.

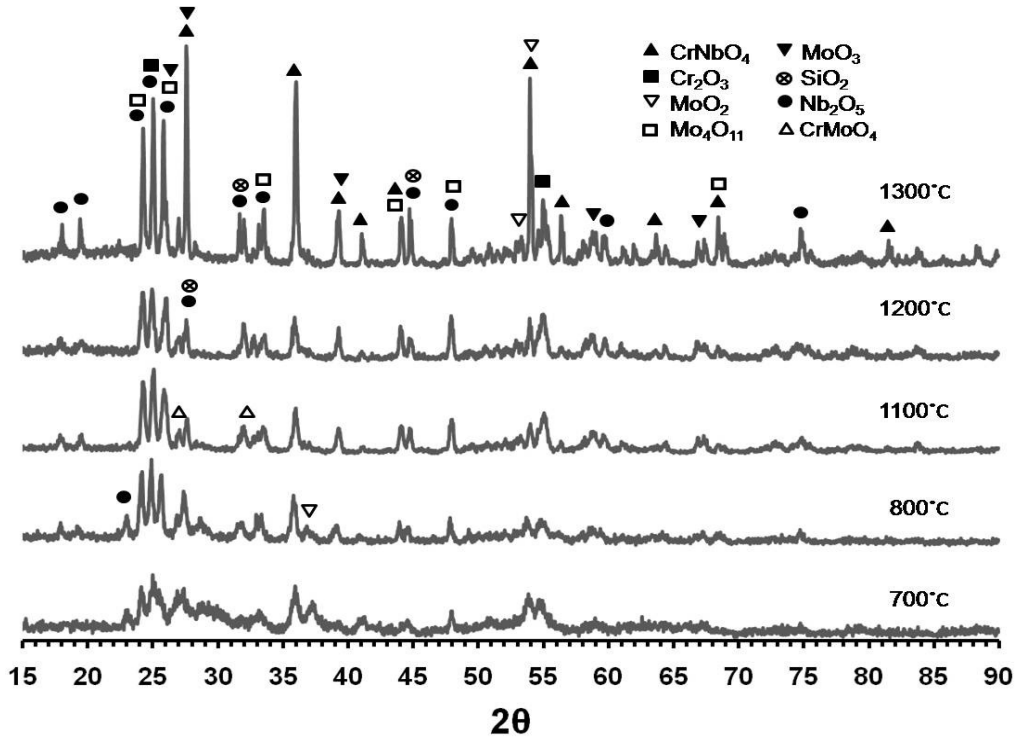

Figure 4.15. XRD patterns of the oxidized products obtained after 24 hours of exposure at 700-1300°C.

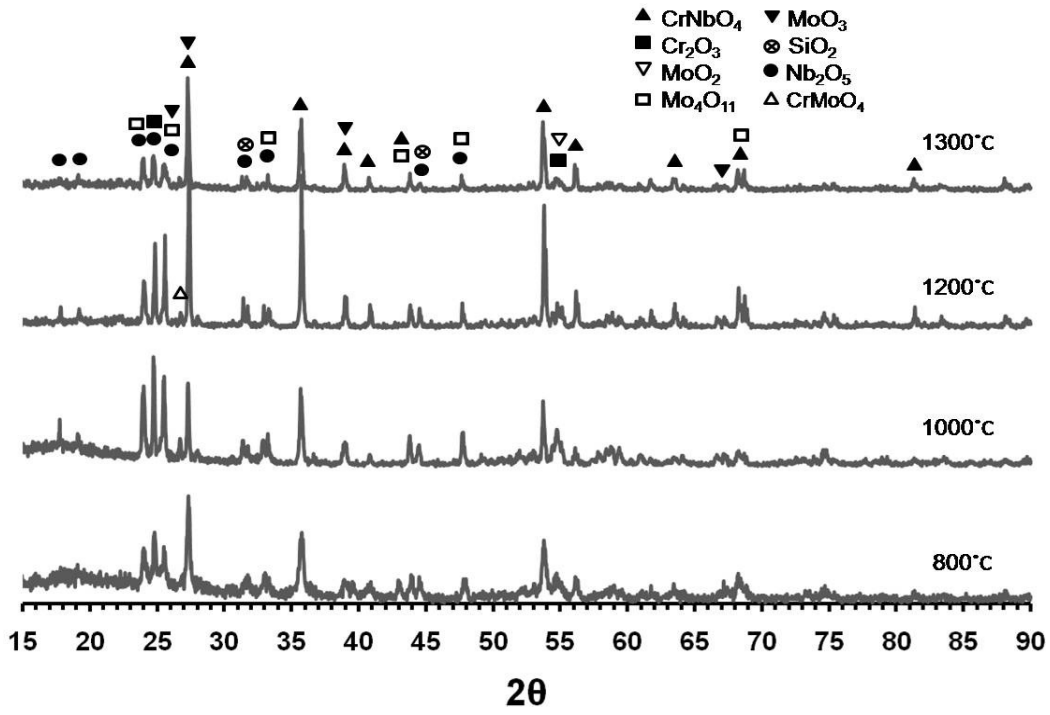

Figure 4.16. XRD patterns of the oxidized products obtained after oxidizing samples in six cycles up to 24 hours at 800, 1000, 1200 and 1300°C.

Table 4.4. Summary of oxides identified by XRD formed during short term oxidation.

Temperature (C°)	Oxides identified by XRD
700	Nb_2O_5 orthorhombic, Nb_2O_5 monoclinic, SiO_2, MoO_3, MoO_2, $CrNbO_4$, Cr_2O_3
800	Nb_2O_5 orthorhombic, Nb_2O_5 monoclinic, SiO_2, MoO_2, $CrNbO_4$, Cr_2O_3
1000-1100	Nb_2O_5 monoclinic, SiO_2, $CrMoO_4$, Mo_4O_{11}, $CrNbO_4$
1200-1300	Nb_2O_5 monoclinic, SiO_2, MoO_3, MoO_2, Mo_4O_{11}, $CrMoO_4$, $CrNbO_4$, Cr_2O_3

4.3 Long Term Oxidation, LTO

Long term oxidation studies consisted of seven cycles of 24 hours, which gave a total exposure time of 168 hours in air at temperatures ranging from 700-1300℃. Figures 4.17 and 4.18 represent the long term curves obtained by plotting the mass gain per unit area as a function of oxidation time at 700-900℃ and 1000-1300℃, respectively. Oxidation kinetics revealed linear and parabolic behaviors at different temperatures and at different interval of time. Both oxidation rates were calculated by the method previously mentioned. Equation 4.1 was used to calculate the parabolic oxidation rate constant (k_p) and linear oxidation rate constant (k_l) was calculated using the equation

$$\left(\frac{\Delta m}{A}\right) = k_l t \tag{4.2}$$

where, Δm is the mass change of the specimen, A is the surface area and t is the exposure time. The parabolic and linear oxidation rate constants of the alloy as well as the mass gain after 168 hours at different temperatures are given in Table 4.5.

At 700℃, the alloy followed a linear oxidation throughout the entire exposure time. A faceted oxide and metal was the end oxidation product. The alloy exhibited linear oxidation for the first 120 hours at 800℃. This linear rate was less than the one

observed at 700℃. Further exposure, more than 120 hours, resulted in a rapid increment of the mass gain. At the end of the oxidation test, the sample disintegrated completely into powder and the most mass gain per unit area (223.1 mg/cm^2) was displayed at this temperature.

Oxidation at 900℃ followed a linear rate for the first 72 hours and for the next two cycles (up to 120 hours) a rapid mass gain per unit area was experimented by the alloy. Further exposure resulted in mass loss. At 900℃, the alloy gained the second most significant mass gained (191.2 mg/cm^2) when compared to other temperatures. At 1000℃, the oxidation kinetics of the alloy was linear during the entire oxidation test. Bulky oxide with no metal was the end product of alloy oxidized at 900 and 1000℃. Alloy followed a parabolic rate at 1100-1300℃. This parabolic rate was only observed in the first 72 hours of oxidation at 1100, while at 1200 and 1300℃ it was maintained throughout the entire oxidation test. At 1100℃ the alloy was completely oxidized. The oxidation product obtained was a swollen bulky oxide with no metal. Alloy showed better oxidation resistance at 1200 and 1300℃ since the least mass gained of 48.3 mg/cm^2 was observed at 1200℃, followed by 1300℃ with a value of 71.3 mg/cm^2. Also, the parabolic rates decreased when compared to short term oxidation. A thick oxide scale surrounding the metal was the end product at these two temperatures. Several cracks were observed in the oxide scale. The oxide scale formed at 1200-1300℃ was slightly deformed, and cracks parallel to the surface of the oxide were noticed.

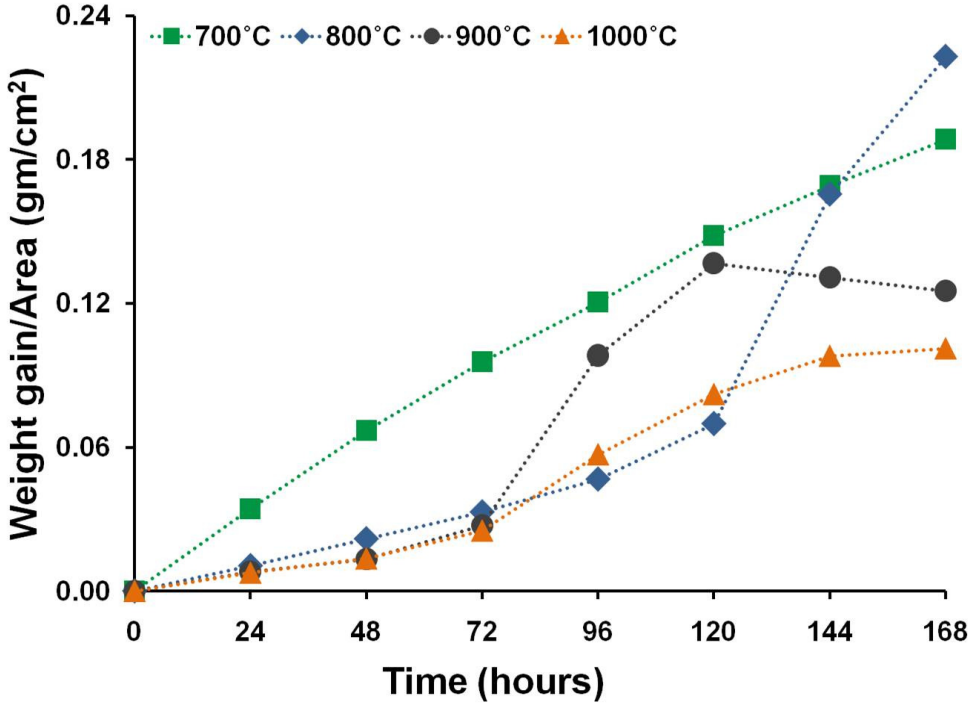

Figure 4.17. Long term oxidation curve (weigh gain per unit area vs. oxidation time) obtained after 168 hours of exposure in air at 700, 800, 900 and 1000℃.

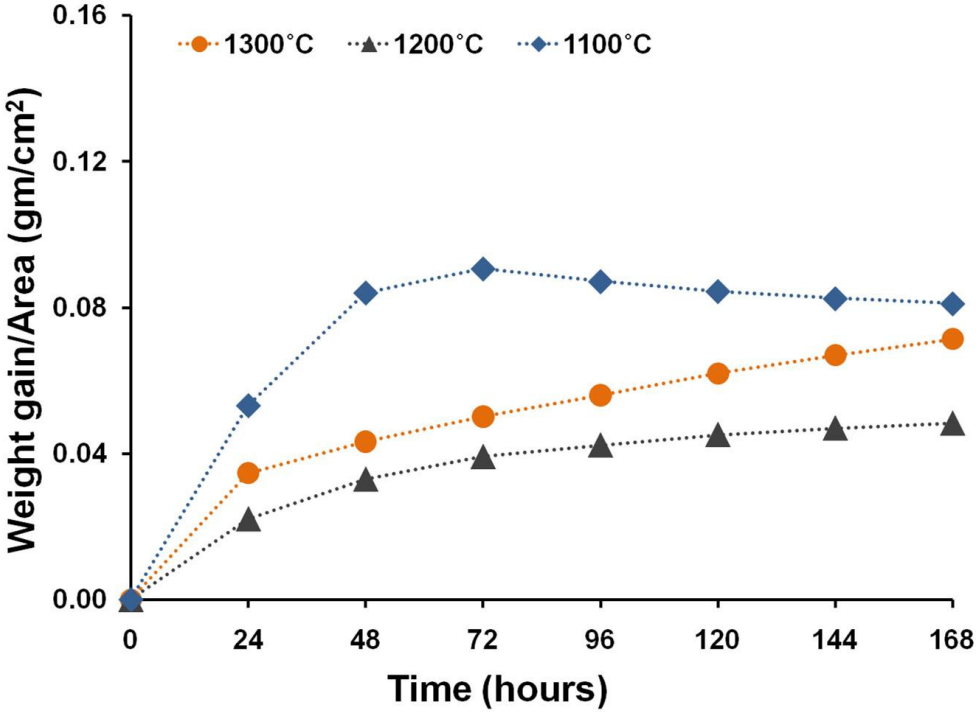

Figure 4.18. Long term oxidation curve (weigh gain per unit area vs. oxidation time) obtained after 168 hours of exposure in air at 1100, 1200 and 1300℃.

Table 4.5. Oxidation rate constants and mass gained after 168 hours of exposure at 700-1300°C.

Temperature (C°)	Total mass gain per area	Oxidation rate constant		R^2
	m (mg/cm^2)	k_l (mg/cm^2/hr)	k_p (mg^2/cm^4/hr)	
700	188.5	1.2	-	0.986
800	223.1	0.52 (0-120 hr)	-	0.970
900	191.2	0.35 (0-72 hr)	-	0.960
1000	163.6	0.34 (0-72hr)	-	0.980
1100	141.2	-	123.8 (0-72 hr)	0.960
1200	48.3	-	16.1	0.910
1300	71.3	-	31.76	0.980

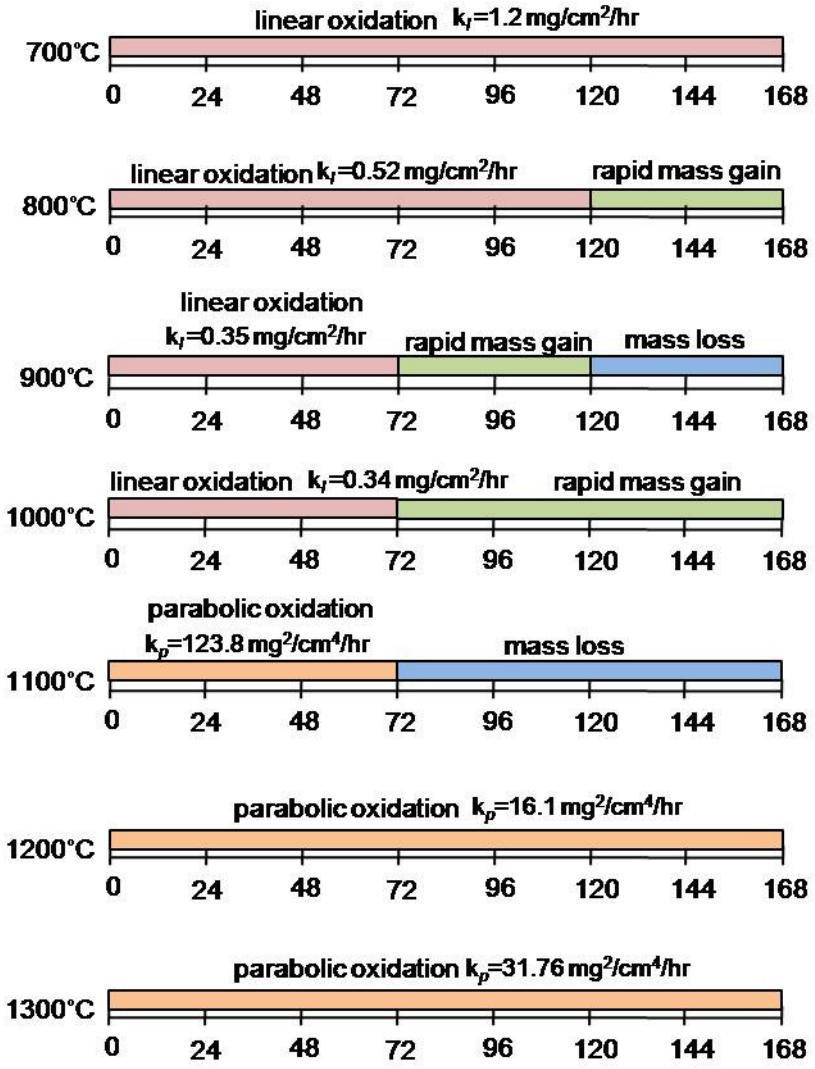

Figure 4.19. Summary of long term oxidation process.

4.3.1 Characterization of Long Term Oxidation Products

4.3.1.1 Scanning Electron Microscopy, SEM

Figure 4.20 shows a BSE micrograph of sample oxidized at 700°C. Elemental analysis on oxides revealed that the scale conforms of a mixture of oxides. A mixture of Nb_2O_5 and MoO_3 are located in the light gray areas, while dark gray areas represent a mixture of SiO_2 and Nb_2O_5. The scale was highly porous with dense oxide mixtures. The scale was thicker than the one formed in short term oxidation. The thickness of the oxide scale was approximately 2mm. The presence of Cr_2O_3 and $CrNbO_4$ was not detected by elemental analysis.

As previously mentioned, the sample oxidized at 1000°C had transformed completely into oxide. Figure 4.21(a) shows an overall view of the oxide formed. The oxide was conformed to regions of chromium and niobium rich oxides. Elemental analysis showed that the white regions of oxide were mainly composed of Nb_2O_5. Gray regions corresponded to the stoichiometry of $CrNbO_4$. The presence of SiO_2 in the oxide scale was not detected by EDS. Figure 4.21(b) illustrates the morphology of these two oxides. The elongated particles correspond to Nb_2O_5 while small round particles are $CrNbO_4$.

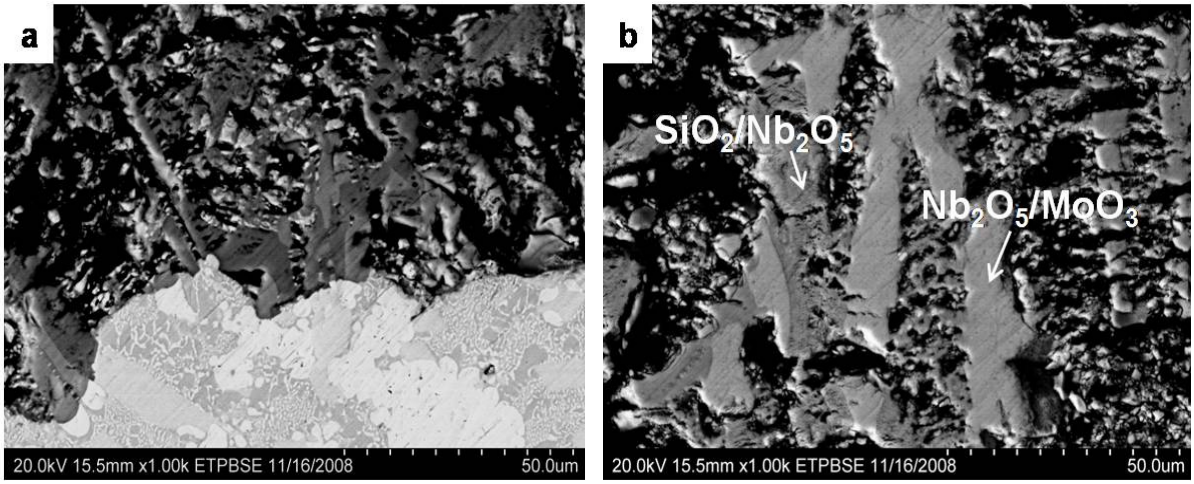

Figure 4.20. BSE images of sample oxidized at 700℃ for 168 hours: (a) shows an overall view of the oxide metal interface. The oxide scale (b) is composed of mixed Nb_2O_5 and MoO_3 (light gray areas) and SiO_2 and Nb_2O_5 (dark gray areas.). Magnification for both micrographs is 1000x.

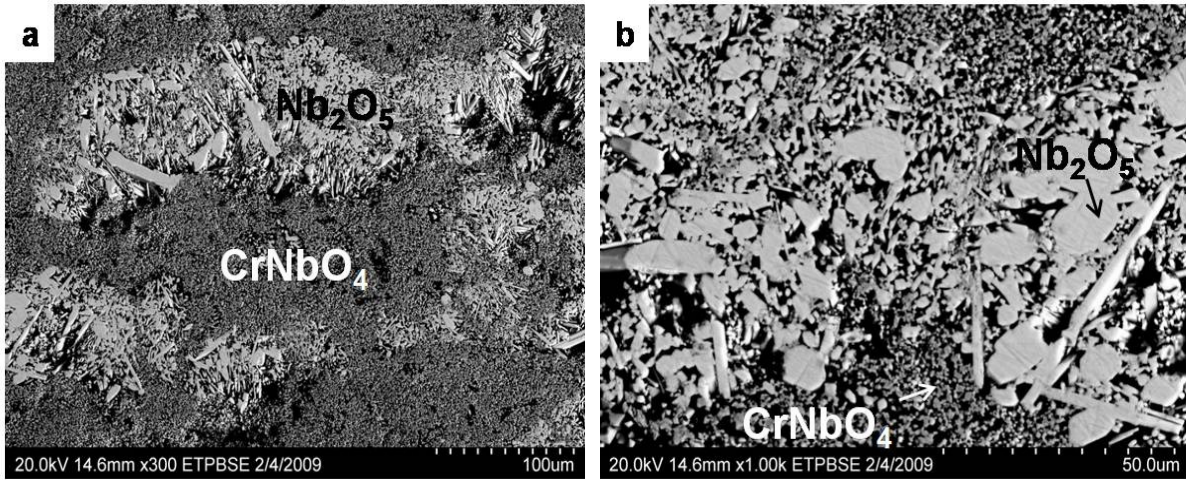

Figure 4.21. BSE micrograph of oxide formed at 1000℃ for 168 hours. Sample completely transformed into oxide at this temperature: (a) is an overall view of oxide scale (300x) while (b) shows the distinct oxides formed and its morphology (1000x).

SEM analysis revealed that sample oxidized at 1200℃ formed two oxide layers and a diffused interface, Figure 4.22(b). Figure 4.22(a) is an overall view of the metal and oxide scale pointing to the two oxide layers formed. First oxide layer in contact with metal, Figure 4.22(c), consists of mixed Nb_2O_5, MoO_2 and MoO_3. Amounts of SiO_2 were also present in this layer. The second layer or outermost layer, Figure 4.22(d) consisted

of Nb_2O_5 and $CrNbO_4$ particles embedded in a SiO_2 matrix. The overall thickness of the oxide scale was 1 mm. The x-ray mappings of these two layers are shown in Figures 4.23 and 4.24. Molybdenum and niobium are richer in the first layer and it is chromium depleted. It can be also observed that the silicon and chromium have higher concentrations in the second layer.

Compared to short term oxidation, sample exposed to long term oxidation at 1300°C also formed a layered oxide scale. Figure 4.25(a) shows an overall view of the oxidized specimen and the location of the three oxide layers. Magnification of micrograph is 80x. Overall thickness of oxide scale is 1.5mm. Figure 4.25(b) shows a high magnification (1000x) micrograph of the diffused oxide-metal interface. Figure 4.25(c) shows the first oxide formed in contact with the metal. The layer 1 is composed of mixture of MoO_2 and MoO_3 (light gray areas) and elongated Nb_2O_5 (gray areas). Silicon dioxide SiO_2 (dark gray areas) matrix was also observed. The layer 2; shown in Figure 4.25(d), consists of globular particles of $CrNbO_4$ (gray areas) oxide embedded in a SiO_2 matrix (black areas). Figure 4.25(d) illustrate the outermost layer, layer 3, formed in alloy. This layer is mainly composed of Nb_2O_5 particles (white areas) with regions or spots of $CrNbO_4$ (gray areas) embedded in a SiO_2 matrix (black areas).

The x-ray mappings performed on layer 1-3 are shown in Figures 4.26 through 4.28 respectively. The location of oxides can be clearly distinguished. In layer 1, dark and gray particles represent the mixture of niobium and molybdenum rich oxides and higher silicon concentration surrounds the particles. The middle oxide layer or layer 2 is clearly composed of particles rich in niobium and chromium. This layer is molybdenum

depleted. The outermost layer is a combination of niobium, chromium and silicon and Si oxides. The matrix is silicon rich and the white areas are higher in niobium concentration, while chromium contrast is observed in the dark regions. Oxygen concentration is located throughout the entire oxide scale.

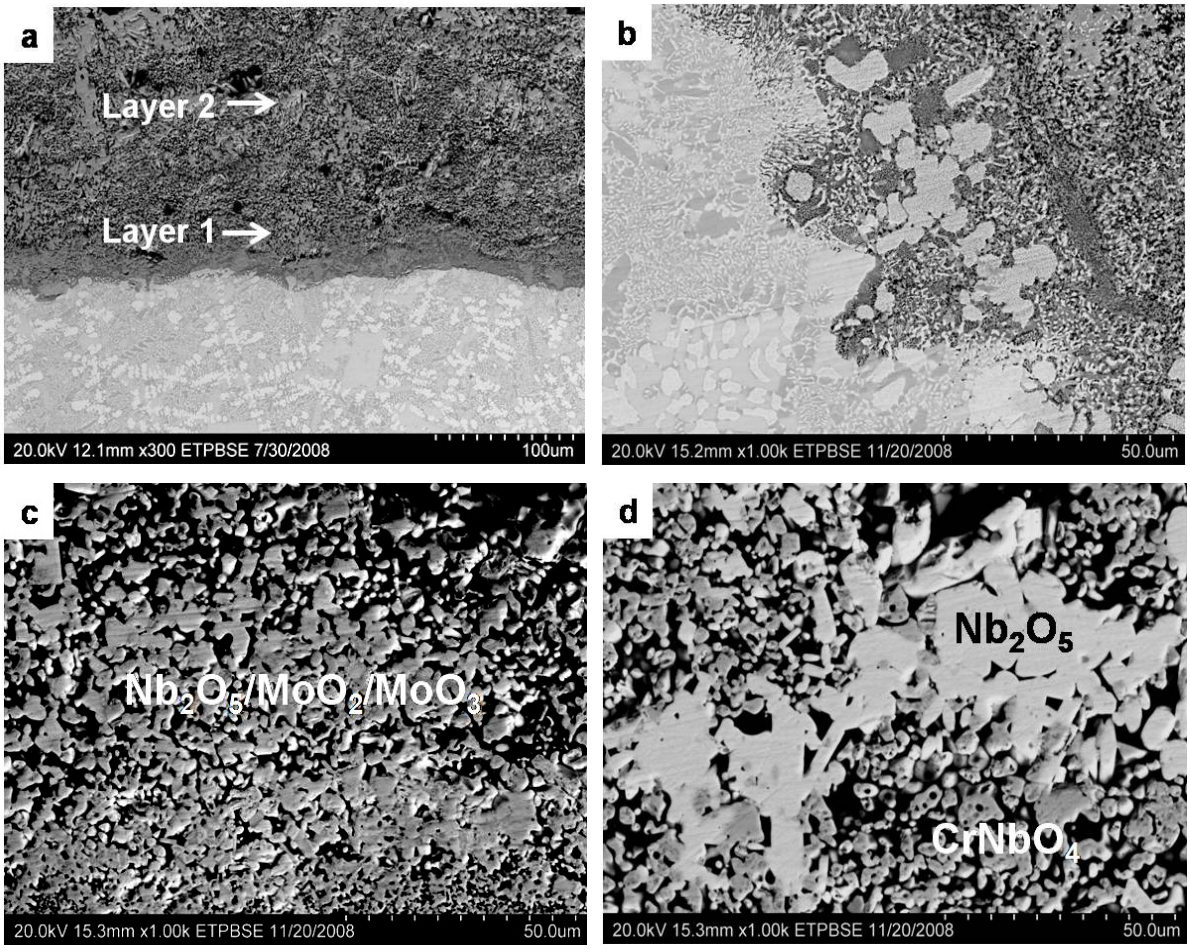

Figure 4.22. BSE micrographs of alloy oxidized at 1200℃ for 168 hrs: (a) shows the oxide metal interface formed at this temperature, (b) illustrates the first oxide layer in contact with metal. This layer consists of MoO_3, Nb_2O_5 and SiO_2, while outermost layer (c) is formed by globular particles of $CrNbO_4$, elongated particles of Nb_2O_5 in a SiO_2 matrix. Magnification of micrographs is 1000x.

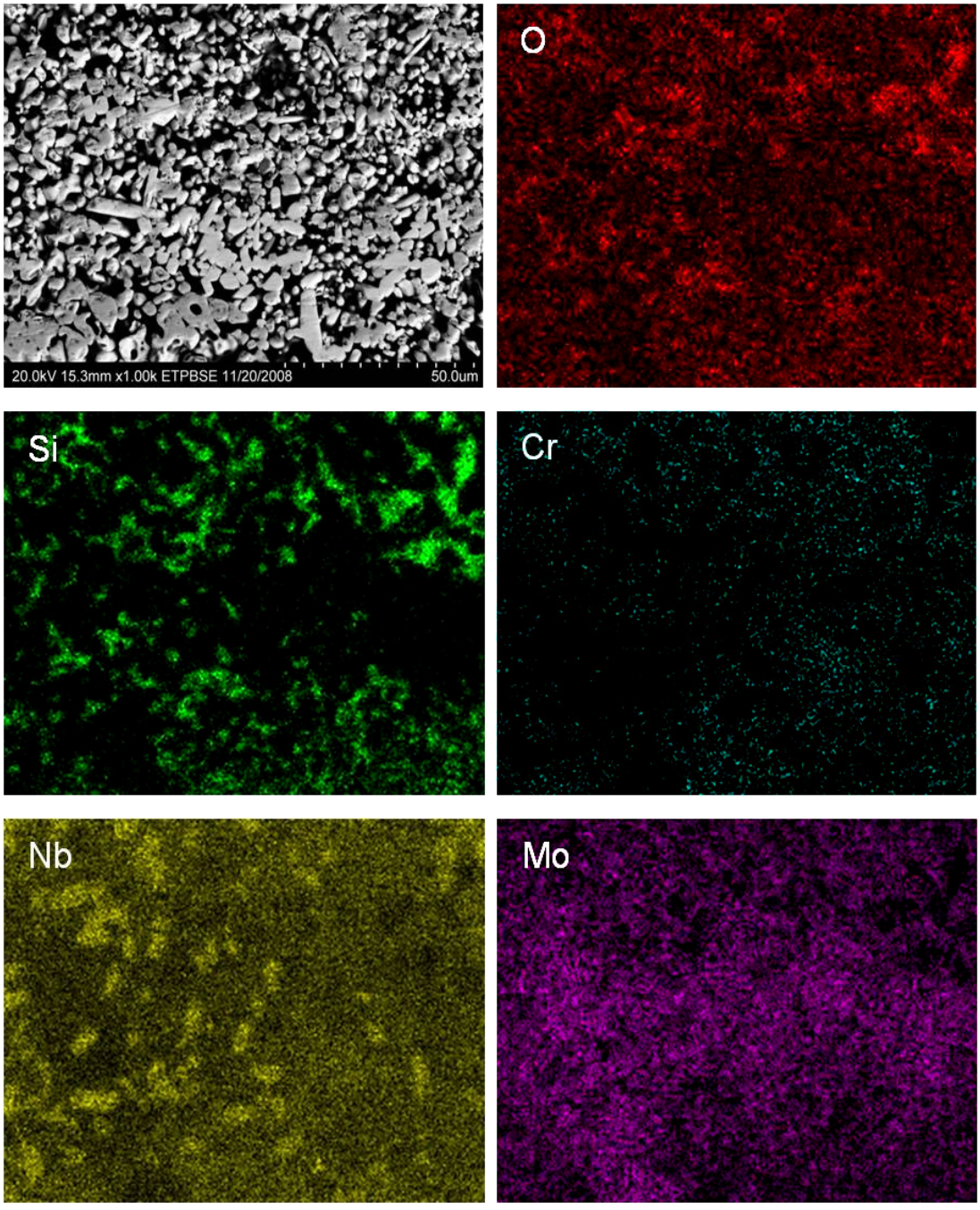

Figure 4.23. Elemental x-ray mapping of O, Si, Cr, Nb and Mo performed on the first oxide layer in contact with metal formed at 1200℃ after 168 hours of exposure.

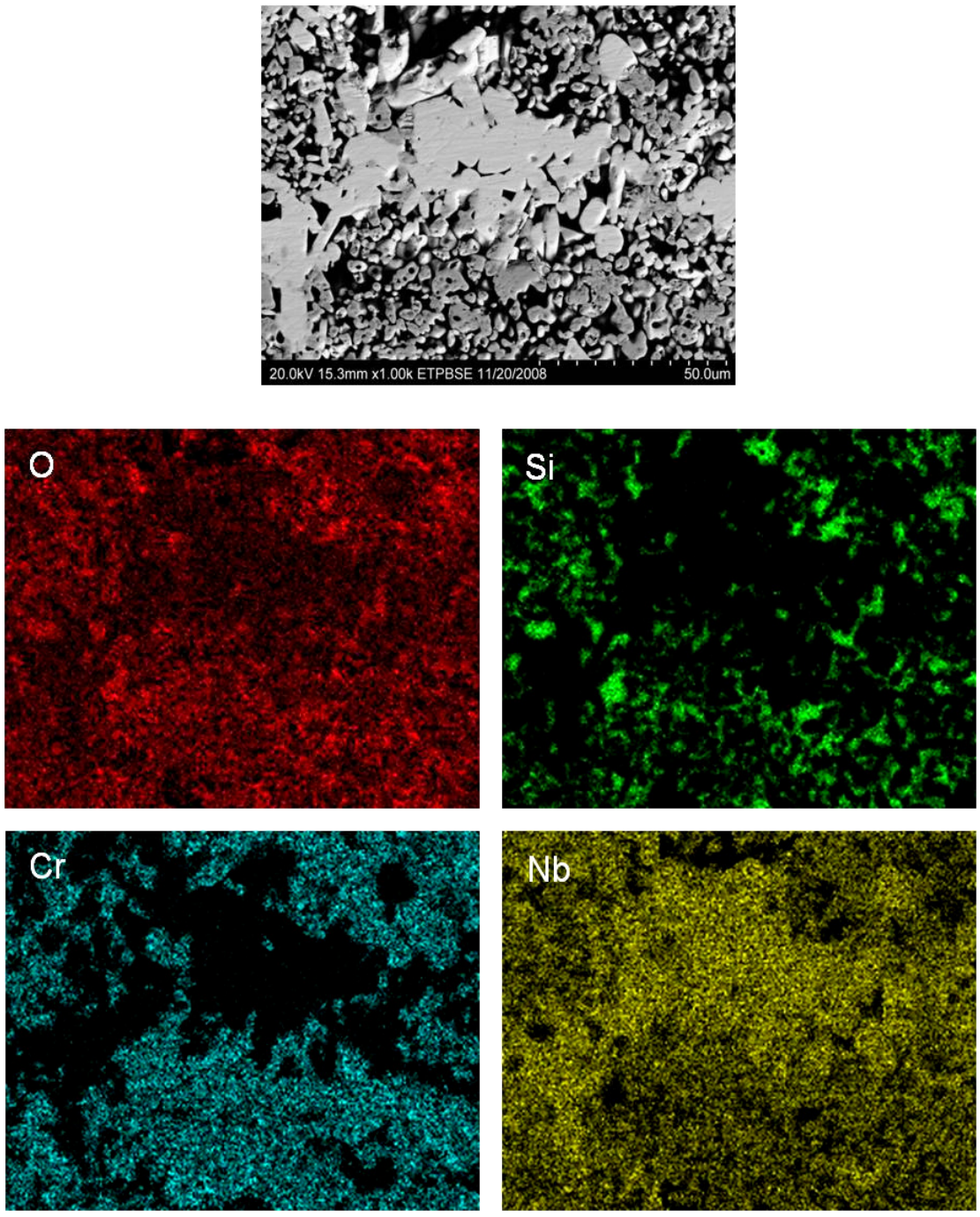

Figure 4.24. Elemental x-ray mapping of O, Si, Cr and Nb performed on the second or outermost oxide layer formed at 1200°C after 168 hours of exposure.

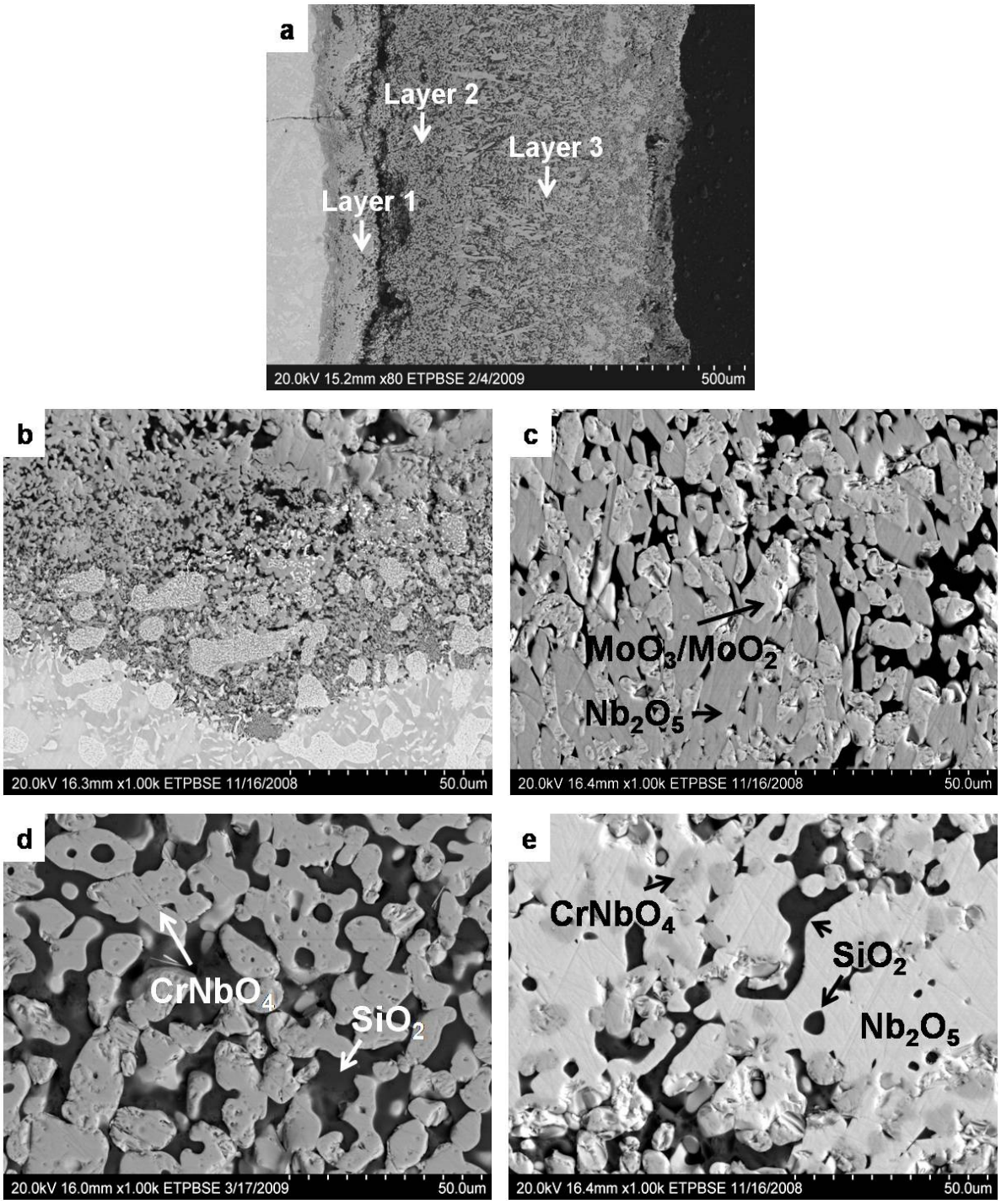

Figure 4.25. BSE micrographs of alloy oxidized at 1300℃ for 168 hrs: (a) shows on overall view of the oxidized sample and the three oxide layers formed, (b) illustrates the diffuse oxide-metal interface. Layer 1 (b) consists of MoO_3, Nb_2O_5 and SiO_2, while layer 2 (d) is formed by globular particles of $CrNbO_4$ embedded in SiO_2 matrix. Layer 3 (d) shows particles of Nb_2O_5 with $CrNbO_4$ regions in a SiO_2 matrix. Magnification of micrographs is (a) 80x and (b-e) 1000x.

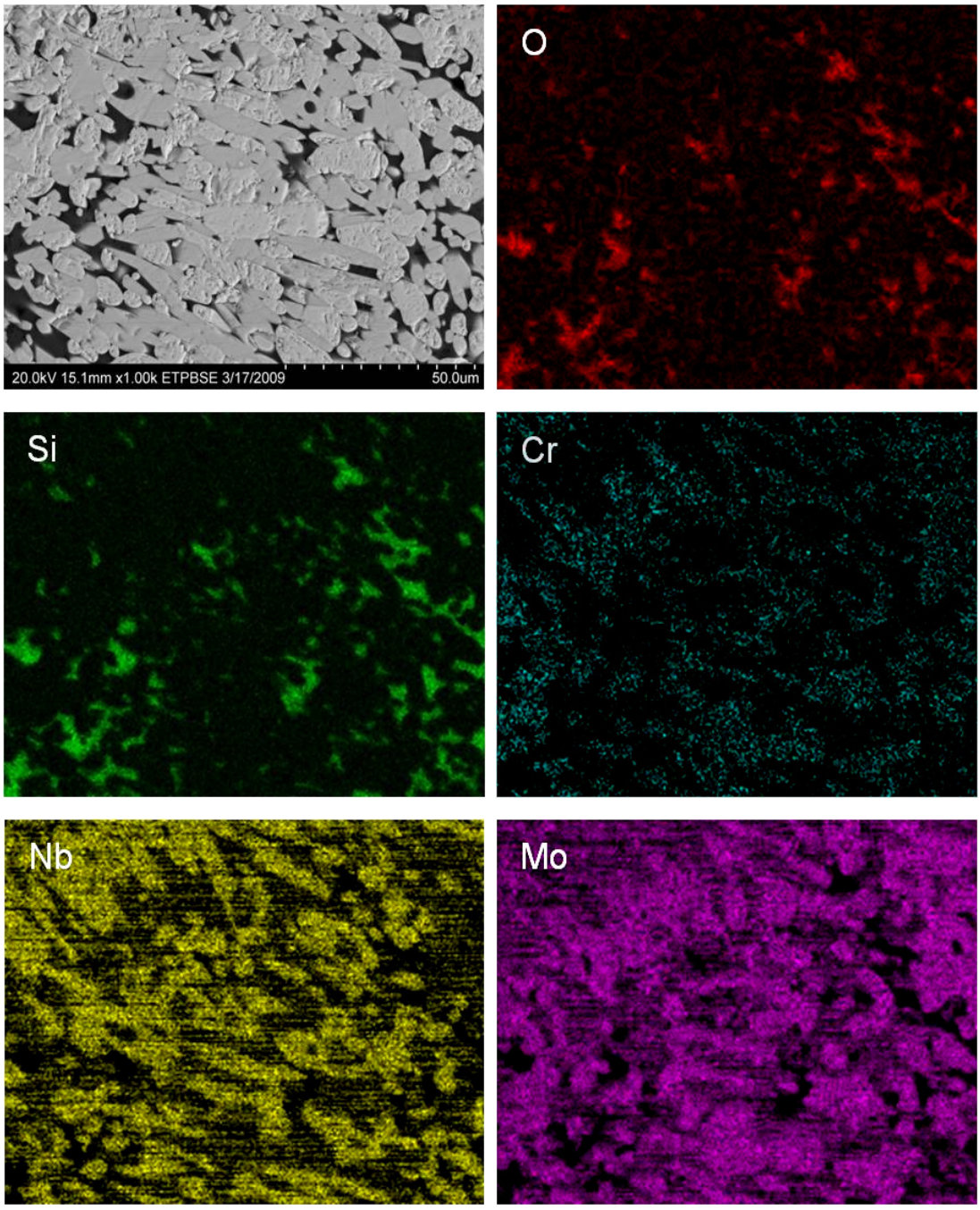

Figure 4.26. Elemental x-ray mapping of O, Si, Cr, Nb and Mo performed on the first oxide layer, layer 1, in contact with metal formed at 1300℃ after 168 hours of exposure.

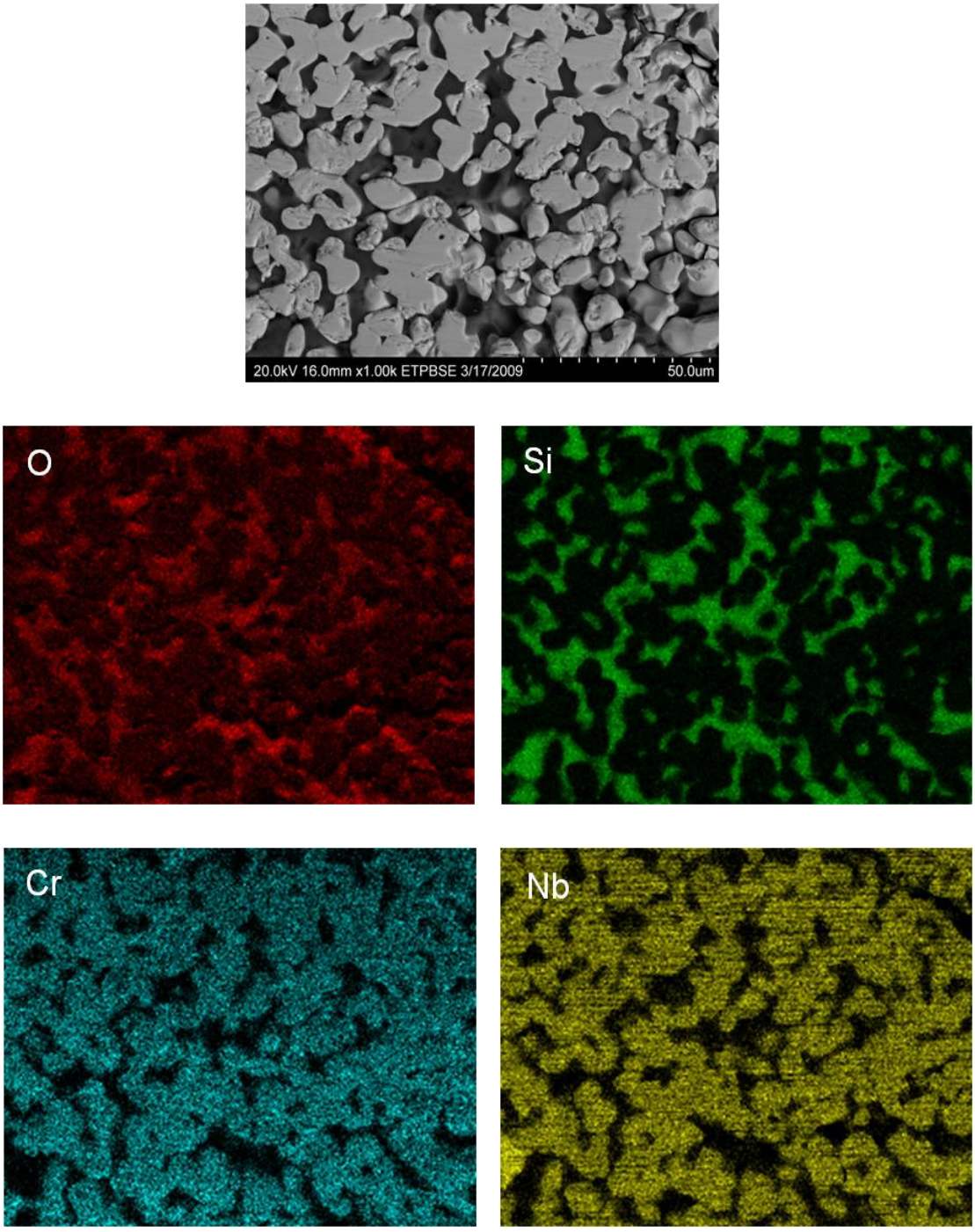

Figure 4.27. Elemental x-ray mapping of O, Si, Cr and Nb performed on the middle oxide layer, layer 2, formed at 1300℃ after 168 hours of exposure.

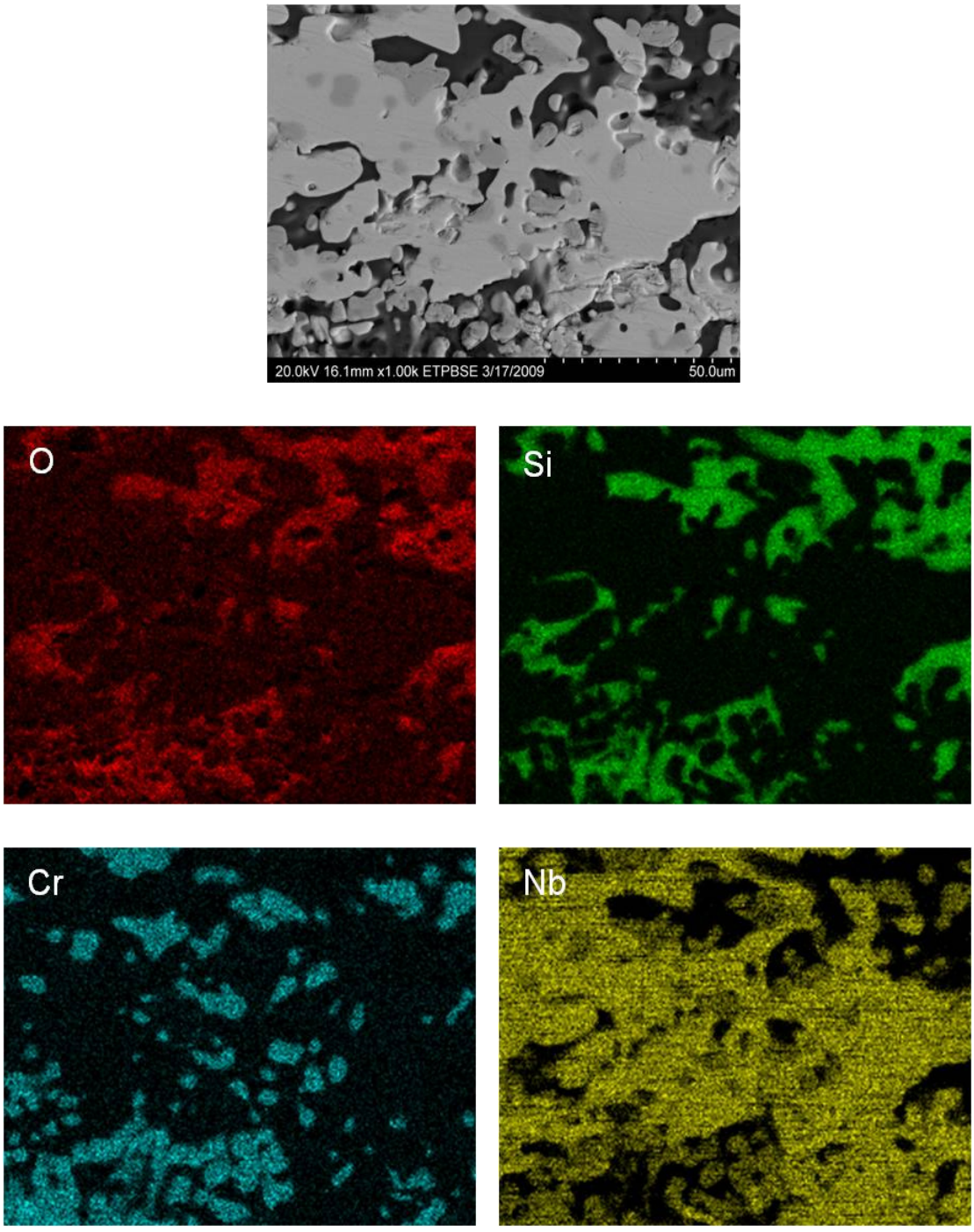

Figure 4.28. Elemental x-ray mapping of O, Si, Cr and Nb performed on the outermost oxide layer, layer 3, formed at 1300°C after 168 hours of exposure.

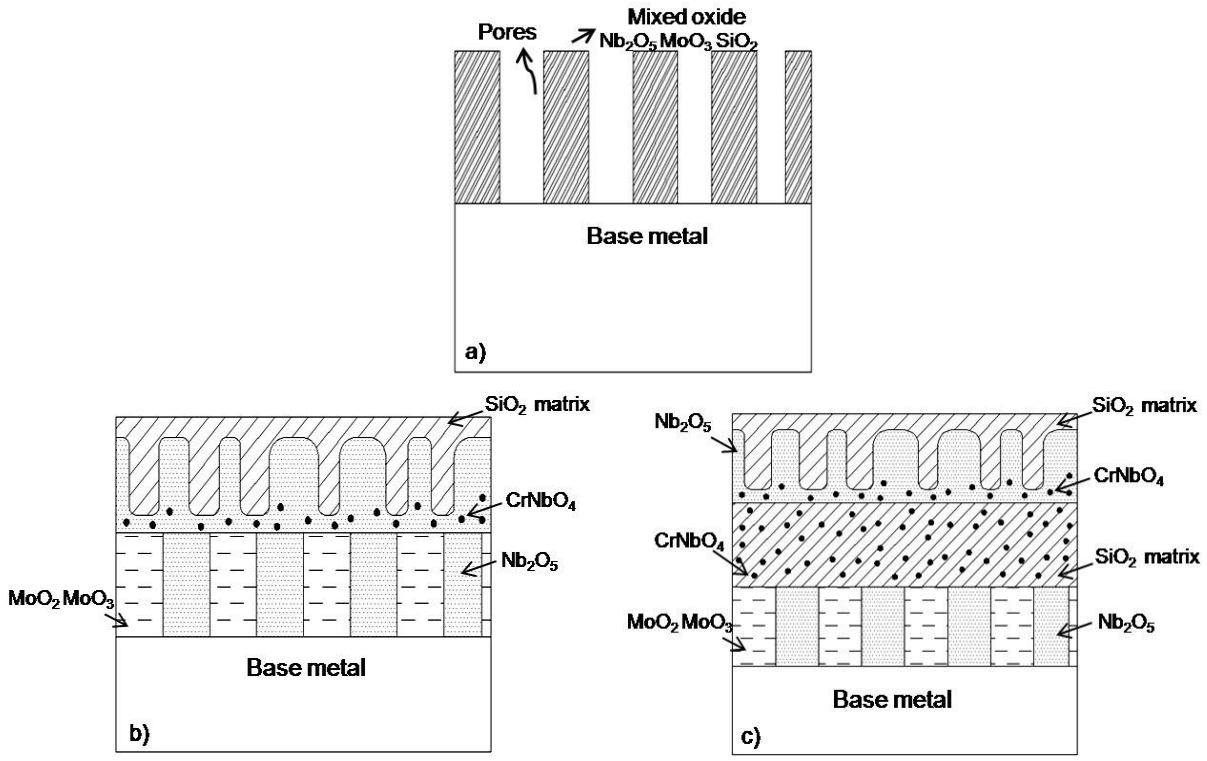

Figure 4.29. A schematic representation for oxide layers formed in samples oxidized at a) 700°C, b) 1200°C and c) 1300°C after 168 hours of exposure. The overall thickness of the oxide scale was a) 2 mm, b) 1 mm and c) 1.5 mm.

4.3.1.2 X-Ray Diffraction, XRD

The oxidation products obtained after 168 hours of exposure were characterized by XRD. Figure 4.30 presents the XRD patterns of oxides obtained from samples oxidized at 700-1300°C. XRD analysis confirmed the presence of Nb_2O_5, $CrNbO_4$, Mo_4O_{11}, MoO_3, MoO_2, $CrMoO_4$ and SiO_2. The predominant oxides formed at all temperatures were $CrNbO_4$ and Nb_2O_5. XRD patterns were similar at all temperatures except at 700°C. An extra peak of orthorhombic Nb_2O_5 appeared at 2θ values of 23° and 29°. No orthorhombic Nb_2O_5 was observed at 800°C.

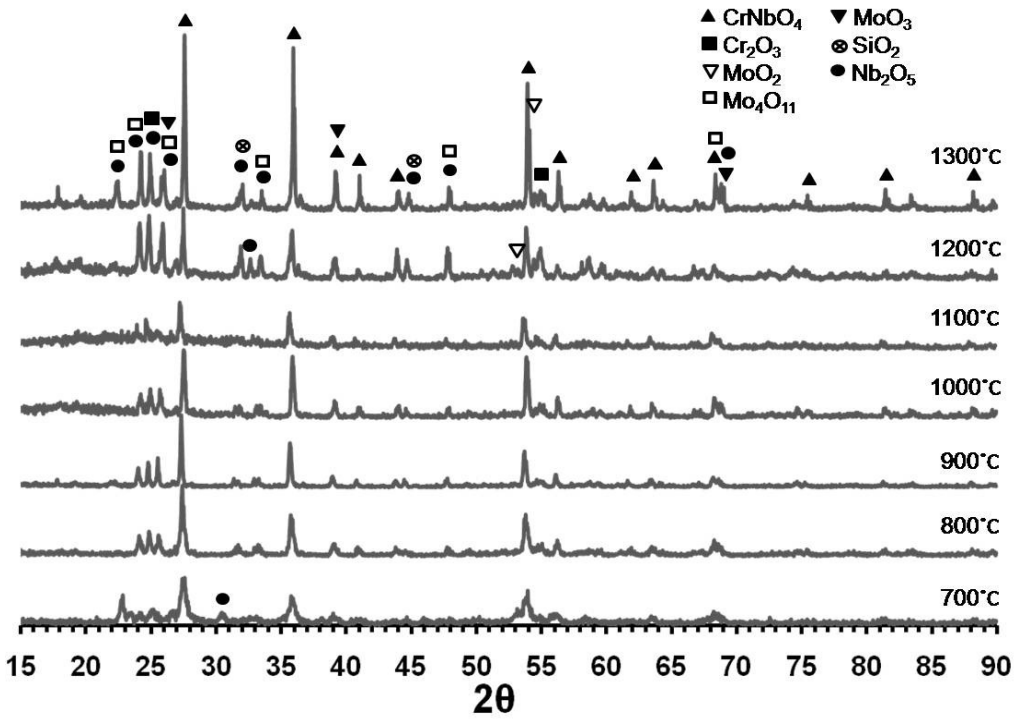

Figure 4.30. XRD pattern of oxides obtained after 168 hours of exposure at 700-1300°C.

4.4 Oxidation Kinetics

Linear oxidation occurs when the metal's surface is not protected by a layer of oxide; with prolonged time exposure the metal would continue to oxidize at a constant rate and it would never slow down causing the destruction of the metal. The formation of volatile or molten oxides, spallation or breakaway of oxides due to growth and internal stresses or the growth of porous non protective oxide are some of the factors that cause linear oxidation. Parabolic oxidation is controlled by the diffusion of atoms and the driving force is the chemical potential. If a compact layer of protective oxide is formed and it continues to grow at prolonged time exposure, the diffusion distance of atoms increases causing a decrement in the diffusion rate. This type of oxidation is of great importance because the oxide growth occurs with a decreasing oxidation rate. Table 4.6 shows a

comparison between parabolic and linear oxidation rate constants of the studied alloy and Nb alloys being developed for high temperature applications. The comparison of the values indicates that studied alloy is competitive compared to other Nb-based alloys previously reported.

Table 4.6. Comparison of parabolic and linear oxidation rate constants between studied alloy and Nb alloys.

Temperature (C°)	Studied Alloy	Oxidation rate constant		Reference
		k_p ($mg^2/cm^4/hr$)	k_l ($mg/cm^2/hr$)	
800	Nb-20Mo-15Si-5B-20Cr	4.84 (0-24 hr)	0.52 (0-120 hr)	This work
	Nb-18Si-5Cr-5Al-5Mo	-	684 (<56 hr)	[3]
	Nb-24Ti-18Si-5Cr-5Al-5Mo	-	205.2(<110 hr)	[3]
	Nb-38Ti-12Hf-12Al	3.3 (<10 hr)	-	[61]
	Nb-18Si-26Mo	746.7 (6-24 hr)	-	[52]
1000	Nb-20Mo-15Si-5B-20Cr	16.64 (0-24 hr)	0.61 (0-72 hr)	This work
	Nb-11Si-2B	20.3 (<10 hr)	-	[55]
	Nb-15Si-2B	115 (<10 hr)	-	[55]
1150	Nb-13Si-4Mo	203.1 (1-24 hr)	-	[52]
	Nb-12Si-15Mo	166 (5-19 hr)	-	[52]
1200	Nb-20Mo-15Si-5B-20Cr	54.15 (0-24 hr) 16.1 (0-168 hr)	-	This work
	Nb-24Ti-18Si-5Cr-5Al-2Mo-5Hf	396 (<110 hr)	-	[3]
	Nb-25Ti	55.8 (<10 hr)	-	[61]
	Nb-38Ti-12Hf-12Al	248.7 (<10 hr)	-	[61]
1300	Nb-20Mo-15Si-5B-20Cr	143.7 (0-24 hr) 31.76 (0-168 hr)	-	This work

4.5 Summary and Discussion of Results

This work presents the results obtained from the studies of the microstructure and high temperature oxidation behavior of the Nb-20Mo-15Si-5B-20Cr alloy.

The as cast microstructure of the alloy, Figure 4.1, consisted of the solid solution (α), the silicides Nb_5Si_3 and Nb_3Si, the Laves phase $NbCr_2$ and the eutectic like microconstituent formed by (α), Nb_3Si and $NbCr_2$. XRD analysis performed on the alloy, Figure 4.3, confirms the presence of these phases as well as their crystal structures.

Solid solution (α) has a BCC structure and Nb_3Si exhibited a tetragonal structure. Laves phase $NbCr_2$ was present in the alloy in the hexagonal C-14 form and tetragonal. Nb_5Si_3 was present in a tetragonal form. Pandat^{TM} 8.1 software also confirmed the presence of (α), Nb_5Si_3 and high temperature C-14 Laves phase $NbCr_2$ and showed that the alloy remains in the four-phase region at different temperatures, see Figure 4.4. The presence of Nb_3Si in the as cast microstructure suggests that equilibrium microstructure was not reached during alloy solidification [3, 5, 7].

Short term oxidation, 24 hours of exposure, suggests that oxidation resistance is temperature dependent. Better oxidation resistance was observed at 900 and 1000°C as shown in Figure 4.5. This behavior can be attributed to the volatilization of molybdenum oxides. The oxidation product formed at 900 and1000°C was a thin oxide layer composed of $CrNbO_4$, Nb_2O_5 and a mixture of SiO_2 and $CrMoO_4$. The oxide layer formed at 1000°C also revealed the presence of Cr_2O_3. As previously mentioned, MoO_3 volatilizes from 400 to 900°C (23, 52). MoO_3 was not detected by SEM and EDS analysis, Figure 4.7(b-d) and Table 4.3 respectively, of samples oxidized at those temperatures. X-ray mapping at 800 and 1000°C shows the existence of Mo in the oxide scale suggesting that molybdenum oxides, such as Mo_4O_{11} and $CrMoO_4$, conforms the oxide scale and not MoO_3. The presence of these oxides was confirmed by XRD analysis, Figures 4.15 and 4.16.

The mass gain per unit area was constant from 1100-1300°C. Analysis of the oxide scale at those temperatures revealed that the oxide scale formed at 1300°C differs from the ones formed at 1100 and 1200°C. The porosity of the oxide scale was reduced and

it exhibited a layered fashion, Figure 4.9. The oxide scale consisted of three dense oxide layers. The layer 1 is composed of molybdenum and niobium oxides, MoO_3, MoO_2, and Nb_2O_5. The layer 2 is formed by $CrNbO_4$ particles embedded in a SiO_2 matrix. The layer 3 shows elongated particles of Nb_2O_5 with some regions of $CrNbO_4$ embedded in SiO_2 matrix. The formation of a SiO_2 matrix and molybdenum oxides was only observed at this temperature. The presence of molybdenum oxides in the layer close to the oxide-metal interface can be attributed to the oxide entrapment caused by the other layers or to formation during cooling [24]. The accumulation of MoO_3 in layer 1 below layer composed of $CrNbO_4$ and SiO_2 matrix indicated that layer 2 may have acted as a diffusion barrier for highly volatile MoO_3. This phenomenon has also been reported in alloys from the Nb-Mo-Si-B and Mo-Si-B systems [55-60].

Detailed oxidation experiments at 800, 1000, 1200 and 1300°C revealed that the oxidation behavior followed a parabolic trend. Better oxidation resistance was observed at 800°C. This can be attributed to spallation of the oxide scales during cooling. The oxidation product at 800°C consisted of a thin oxide scale with no powder and at higher temperatures the oxide layer detached from the metal causing further oxidation of the alloy.

The oxidation products at all temperatures are a mixture of $CrNbO_4$, Nb_2O_5 and SiO_2 among others; the predominant oxides formed at all temperatures were $CrNbO_4$ and Nb_2O_5 (refer to Table 4.5.).

Long term oxidation, 168 hours of exposure, shows that oxidation resistance is time dependent. Better oxidation resistance was observed at 1200 and 1300°C at the end of

168 hours. Oxidation at 700℃ followed a linear oxidation throughout the entire test. Oxidation at 900 and 1000℃ followed a linear behavior for the first 72 hours. Further exposure resulted in complete oxidation of sample. A parabolic trend was observed from 1100-1300℃. Complete oxidation was observed in sample oxidized at 800℃. The sample was completely transformed into powder at the end of 168 hours indicating that pesting had occurred. Pesting oxidation is observed at intermediate temperatures and it preferentially attacks the intermetallic compounds. Pesting is characterized by the disintegration of alloys into small oxide particles and powder [25]. Complete sample oxidation was also observed at 900-1100℃. Analysis of oxide scales formed at 1200 and 1300℃ revealed the presence of different layers of oxides, Figures 4.22 and 4.25 respectively. The presence of SiO_2 matrix was observed at those temperatures. The improved oxidation resistance at higher temperatures can be attributed to the formation of SiO_2 matrix and CrNbO4 particles. The combination of these two oxides acted as a barrier to prevent the alloy from further oxidation. Even though $CrNbO_4$ was the predominant oxide formed at all temperatures, its protective nature was not sufficient to prevent the alloy's complete oxidation from 800-1100℃. Also, the formation of Nb_2O_5, a non-protective oxide, was too dominant to prevent complete oxidation of samples.

CHAPTER 5

CONCLUSIONS

- The microstructure of as cast Nb-20Mo-15Si-5B-20Cr alloy consists of four phases: Solid solution (α), silicides Nb_5Si_3 and Nb_3Si, Laves phase $NbCr_2$ and the eutectic like microconstituent (α), Nb_3Si and $NbCr_2$.
- The crystal structures of phases are: BCC (α), tetragonal Nb_3Si, hexagonal $NbCr_2$ and tetragonal Nb_5Si_3.
- Calculated isothermal sections showed that phases present in alloy remain stable at all temperatures.
- The presence of Nb_3Si in the as cast microstructure suggests that equilibrium microstructure was not reached during alloy solidification.
- Short term oxidation is temperature dependent.
- Short term oxidation curve showed that better oxidation resistance was displayed at 900 and 1000°C.
- $CrNbO_4$, Nb_2O_5 and SiO_2 were the main oxides present in oxide scales at all temperatures.
- The short term oxidation kinetics follows a parabolic behavior.
- Long term oxidation is time dependent.
- Samples oxidized at 1200 and 1300°C showed better oxidation resistance.
- Complete sample oxidation was observed in samples oxidized from 800-1100°C.
- Pesting oxidation behavior was exhibited by sample oxidized at 800°C.
- Oxidation kinetics followed a linear behavior from 700-1000°C and a parabolic behavior from 1100-1300°C.

- The presence of silicon oxide matrix and MoO_3 was observed at 1200 and 1300℃. The combination of $CrNbO_4$ and SiO_2 matrix provided oxidation resistance to the alloy.
- Parabolic and linear oxidation rate constants, obtained at 800, 1000, 1200 and 1300℃ for both short and long term oxidation are competitive compared to the values for Nb-based alloys reported by different authors.

REFERENCES

[1] B.P. Bewlay, M.R. Jackson, J.-C. Zhao, and P.R. Subramanian. “A review of very-high-temperature Nb-silicide-based composites.” *Metall. Mater. Trans. A*., 2003, vol. 34A, 2043-2052.

[2] B.P. Bewlay, M.R. Jackson, J.-C. Zhao, P.R. Subramanian, M.G. Mendiratta and J.J. Lewandowski. “Ultrahigh-temperature Nb-silicide-based composites.” *MRS Bulletin*, September 2003, 646-653.

[3] J. Geng, P. Tsakiropoulos, and G. Shao. “Oxidation of Nb-Si-Cr-Al in situ composites with Mo, Ti and Hf additions.” *Mater. Sci. Eng. A*., 2006, vol. 441, 26-38.

[4] B.P. Bewlay. “Very high-temperature Nb-silicide alloys.” *Materials for High Temperature Applications: Next Generation of Super Alloys and Beyond: Refractory Alloys I Symposium*, 138th TMS Annual Meeting, San Francisco Ca, February 2009.

[5] J. Geng, P. Tsakiropoulos, and G. Shao. “The effects of Ti and Mo additions on the microstructure of Nb-silicide based in situ composites.” *Intermetallics*, 2006, vol. 14, 227-235.

[6] K. Zelenistas, and P. Tsakiropoulos. “Effect of Al, Cr, and Ta additions on the oxidation behavior of Nb-Ti-Si in situ composites at 800˚C.” *Mater. Sci. Eng. A*., 2006, vol. 416, 269-280.

[7] J. Geng, P. Tsakiropoulos, and G. Shao. “A study of the effects of Hf and Sn additions on the microstructure of Nb_{ss}/Nb_5Si_3 based in situ composites.” *Intermetallics*, 2007, vol. 15, 69-76.

[8] J. Geng, and P. Tsakiropoulos. “A study of the microstructures and oxidation of Nb-Si-Cr-Al-Mo in situ composites alloyed with Ti, Hf and Sn.” *Intermetallics*, 2007, vol. 15, 382-395.

[9] M.D. Gonzalez, and S.K. Varma. “Oxidation behavior of alloys from the Nb-W-Cr system containing C Modifiers.” *Supplemental Proceedings: Materials Processing and Properties*, 2008, vol. I, 455-460.

[10] M.D. Moricca, and S.K. Varma. “The high-temperature oxidation characteristics of alloys from the Nb-W-Cr system with C additions.” *Journal of Metals*, 2008, vol. 60, no. 7, 66-69.

[11] J. Ventura, B. Portillo, and S.K. Varma. “Oxidation resistant $NbCr_2$ phase in Nb-W-Cr system.” *Article in Press, Journal of Alloys and Compounds*, 2008.

[12] K.S. Chan. “Cyclic oxidation response of multiphase Niobium-based alloys.” *Metall. Mater. Trans. A.*, 2004, vol. 35A, 589-597.

[13] M.P. Brady, J.H. Zhu, C.T. Liu, P.F. Tortorelli, and L.R. Walker. “Oxidation resistance and mechanical properties of Laves phase reinforced Cr in-situ composites.” *Intermetallics*, 2000, vol. 8, 1111-1118.

[14] J. Geng, G. Shao, and P. Tsakiropoulos. “Study of three-phase equilibrium in the Nb-rich corner of Nb-Si-Cr system.” *Intermetallics*, 2006, vol. 14, 832-837.

[15] J.-C. Zhao, M.R. Jackson, and L.A. Peluso. “Determination of the Nb–Cr–Si phase diagram using diffusion multiples.” *Acta Materialia*, 2003, vol. 51, 6395-6405.

[16] A.S Khanna. *Introduction to High Temperature Oxidation and Corrosion*. Metals Park, OH: ASM International, 1993.

[17] S.A. Bradford. “Fundamentals of Corrosion in Gases.” *ASM Metals Handbook*. Formerly 9th edition, vol. 13. Metals Park, OH: ASM International, 1990.

[18] N. Birks, G.H. Meier, and F.S. Pettit. *Introduction to the High-Temperature Oxidation of Metals*. United Kingdom: University Press Cambridge, 2006.

[19] W.H. Whitlock, et al. “High Temperature Alloys.” *Kirk-Othmer Encyclopedia of Chemical Technology*. 5th edition, vol. 13, 2005.

[20] “Chromium Compounds.” *Kirk-Othmer Encyclopedia of Chemical Technology*. 5th edition, vol. 6, 2006.

[21] F. Stott. “Developments in understanding the mechanisms of growth of protective scales on high-temperature alloys.” *Materials Characterization*, 1992, vol. 28, issue 3, 311-325.

[22] F. Stott, G.C. Wood, and J. Stringert. “The influence of alloying elements on the development and maintenance of protective scales.” *Oxidation of Metals*, 1995, vol. 44, 113-145.

[23] “Molybdenum and Molybdenum Alloys.” *Kirk-Othmer Encyclopedia of Chemical Technology*. 5th edition, vol. 17, 2006.

[24] J.W. Semmel, Jr. “The oxidation of Tungsten and Molybdenum from 1800 to 2500˚F.” *High Temperature Materials Conference, Cleveland, OH*. New York: John Wiley & Sons, Inc, 1959, 510-519.

[25] E.M. Savitskii, and G. S. Burkhanov. *Physical Metallurgy of Refractory Metals and Alloys*. New York: Consultants Bureau, 1970.

[26] R.G. Frank. “The present and future of columbium alloys.” *Symposium on Refractory Metals and Alloys, Wayne State University*, 1960, vol. 11, 237-281.

[27] J.W. Pugh. “Refractory metals: Tungsten, Tantalum, Columbium, and Rhenium.” *High Temperature Materials Conference, Cleveland, OH*. New York: John Wiley & Sons, Inc, 1959, 306-318.

[28] Pandat^{TM} 8.1. *Phase diagram calculation software for multicomponent systems*. CompuTherm LLC: Madison, WI 53719, 2009.

[29] M.E. Schlesinger. "The Nb-Si (Niobium-Silicon) system." *Journal of Phase Equilibria*, 1993, vol. 14, 502-509.

[30] K. Chattopadhyay, G. Balachandian, R. Mitra and K.K. Ray. "Effect of Mo on microstructure and mechanical behavior of as-cast Nb_{ss}-Nb_5Si_3 in situ composites." *Intermetallics*, 2006, vol. 14, 1452-1460.

[31] W.-Y. Kim, H. Tanaka, and S. Hanada. "Microstructure and high temperature strength at 1773 K of Nb_{ss}/Nb_5Si_3 composites alloyed with molybdenum." *Intermetallics*, 2002, vol. 10, 625-634.

[32] K. Chattopadhyay, R. Sinha, R. Mitra and K.K. Ray. "Effect of Mo and Si on morphology and volume fraction of eutectic in Nb-Si-Mo alloys." *Mater. Sci. Eng. A.*, 2007, vol. 456, 358-363.

[33] R.W. Fountain, and M. Korchynsky. "Chromium-based alloys for high temperature applications." *High Temperature Materials Conference, Cleveland, OH*. New York: John Wiley & Sons, Inc, 1959, 207-228.

[34] C. Jiang. "Site preference of early transition metals in C15 $NbCr_2$." *Acta Materialia*, 2007, vol. 55, 1599-1605.

[35] M. Fujita, Y. Kaneno, and T. Takasugi. "Phase field and room-temperature mechanical properties of C15 phase in Nb-Hf-Cr and Nb-Ta-Cr alloy systems." *Journal of Alloys and Compounds*, 2006, vol. 424, 283-288.

[36] F. Stein, M. Palm, G. Sauthoff. "Structure and stability of Laves phases. Part I. Critical assessment of factors controlling Laves phase stability", *Intermetallics*, 2004, vol. 12, 713-720.

[37] G. Shao. “Thermodynamic modeling of the Cr-Nb-Si system.” *Intermetallics*, 2005, vol. 13, 69-78.

[38] B.P. Bewlay, Y. Yang, R. L. Casey, M. R. Jackson, and Y. A. Chang. “Effect of Cr addition on the phase equilibria of the Nb-Si system.” *Mater. Res. Soc. Symp. Proc.*, 2007, vol. 980, 1-6

[39] N. David, Y. Cartigny, T. Belmonte, J.M. Fiorani, and M, Vilasi. “Thermodynamic description of the Cr-Nb-Si isothermal section at 1478.” *Intermetallics*, 2006, vol. 14, 464-473.

[40] J.J. Huebsch, M.J. Kramer, H.L. Zhao, and M. Akinc. “Solubility of boron in $Mo_{5+y}Si_{3-y}$.” *Intermetallics*, 2000, vol. 8, 143-150.

[41] J.H. Perepezko, R. Sakidja, and S. Kim. “Phase stability in processing and microstructure control in high temperature Mo-Si-B alloys.” *Mater. Res. Soc. Symp. Proc.*, 2001, vol. 646, N4.5.1-N4.5.12.

[42] M. Kumagai, K. Ito, and M. Yamaguchi. “On Mo-9Si-18B alloys with T_2-Mo_{ss} eutectic microstructure: Mechanical properties and protective silicide coating.” *Mater. Res. Soc. Symp. Proc.*, 2003, vol. 753, BB5.26.1- BB5.26.6.

[43] R. Sakidja, and J.H. Perepezko. “Alloying and microstructure stability in the high-temperature Mo–Si–B system.” *Journal of Nuclear Materials, 2007*, vol. 366, 407–416.

[44] T. Hurlen. “Oxidation of Niobium.” *Journal of the Institute of Metals*, 1961, vol. 89, 273-280.

[45] M.P. Arbuzov, and V. G. Chuprina. “The oxidation of niobium and the structure of niobium oxides.” *Izvestiya VUZ. Fizika*, 1965, No. 2, 129-183.

[46] H. Goldschmidt. “A high-temperature X-ray investigation of niobium pentoxide and some problems concerning the oxidation of Niobium”, *Journal of the Institute of Metals*, 1959, vol. 87, 235-239.

[47] Y. Murayama, and S. Hanada. “High temperature strength, fracture toughness and oxidation resistance of Nb-Si-Al-Ti multiphase alloys.” *Science and Technology of Advanced Materials*, 2002, vol. 3, 145-156.

[48] H.J. Grabke, and M. Schütze. *Oxidation of Intermetallics.* New York: Wiley-VCH, 1997.

[49] S. Paswan, R. Mitra, and S.K. Roy. “Oxidation behavior of the Mo-Si-B and Mo-Si-B-Al alloys in the temperature range of 700-1300˚C.” *Intermetallics*, 2007, vol. 15, 1217-1227.

[50] T. Murakami, S. Sasaki, K. Ichikawa, A. Kitahara. “Oxidation resistance of powder compacts of the Nb-Si-Cr system and $Nb_3Si_5Al_2$ matrix compacts prepared by spark plasma sintering.” *Intermetallics*, 2001, vol. 9, 629-635.

[51] T. Murakami, S. Sasaki, and K. Ito. “Oxidation behavior and thermal stability of Cr-doped $Nb(Si,Al)_2$ and $Nb_3Si_5Al_2$ matrix compacts prepared by spark plasma sintering.” *Intermetallics*, 2003, vol. 11, 269-278.

[52] K. Chattopadhyay, R. Mitra, and K.K. Ray. “Nonisothermal and isothermal oxidation behavior of Nb-Si-Mo alloys.” *Metall. Mater. Trans. A.*, 2008, vol. 39A, 577-592.

[53] K. Ito, T. Murakami, K. Adachi, and M. Yamaguchi. “Oxidation behavior of Mo-9SI-18B alloy pack-cemented in a Si-base pack mixture.” *Intermetallics*, 2003, vol. 11, 763-772.

[54] T. Murakami, C.N. Xu, A. Kitahara, M. Kawahara, Y. Takahashi, H. Inui, and M. Yamaguchi. “Microstructure, mechanical properties and oxidation behavior of powder compacts of the Nb-Si-B system prepared by spark plasma sintering.” *Intermetallics*, 1999, vol. 7, 1043-1048.

[55] V. Behrani, A.J. Thom, M.J. Kramer, and M. Akinc. “Microstructure and oxidation behavior of Nb-Mo-Si-B alloys.” *Intermetallics*, 2006, vol. 14, 24-32.

[56] Y. Liu, M.J. Kramer, A.J. Thom, and M. Akinc. “Oxidation behavior of multiphase Nb-Mo-Si-B intermetallics.: *Metall. Mater. Trans. A*., 2005, vol. 36A, 601-607.

[57] M. Akinc, et al., “Boron-doped molybdenum silicides for structural applications.” *Mater. Sci. Eng. A*., 1999, vol. 261A,16-23.

[58] M.K. Meyer, A.J. Thom, and M. Akinc. “Oxidation scale formation and isothermal oxidation behavior of Mo-Si-B intermetallics at 600-1000˚C.” *Intermetallics*, 1999, vol. 7, 153-162.

[59] M.G. Mendiratta, T.A. Parthasarathy, and D.M. Dimiduk. “Oxidation behavior of a αMo-Mo_3Si-Mo_5SiB_2 (T2) three phase system.” *Intermetallics*, 2002, vol. 10, 225-232.

[60] F. Wang, A. Shan, X. Dong, and J. Wu. “Oxidation behavior of Mo-12.5Si-25B alloy at high temperature.” *Journal of Alloys and Compounds*, 2008, vol. 459, 362-368.

[61] K.S. Chan. “Cyclic-oxidation resistance of Niobium-base in situ composites: Modeling and experimentation.” Oxidation of Metals, 2004, vol. 61, No. 3-4, 165-194.

CURRICULUM VITAE

Julieta Angelica Ventura Luna was born on August 12, 1983 in Celaya, Guanajuato, Mexico. She is the eldest of three daughters of Raul Arnoldo Ventura Loya and Rosa Ma. Luna Ramos. She completed her high school education at Colegio Arturo Rosenblueth, located in Celaya, Guanajuato, Mexico, in May 2001. In the fall of that year she enrolled at The University of Texas at El Paso and graduated in May 2006 with a B.S. degree in Mechanical Engineering. Upon graduation, she immediately enrolled for graduate studies to pursue a M.S. degree in Metallurgical and Materials Engineering. In the summer of 2007 she worked as a graduate intern for Lockheed Martin Space Systems Michoud Operations located in New Orleans, LA. She worked in the Materials Department for NASA's Orion crew exploration vehicle. In the fall of that year she obtained a research assistant position with Dr. S.K. Varma under whom she authored several publications and made a poster and oral presentation at MAES and TMS conferences. She also was awarded with the Ray W. Guard Memorial Award for outstanding graduate student and graduate research.

Permanent Address: 514 Tawny Oak Pl.
El Paso, TX 79912

This thesis was typed by Julieta Angelica Ventura